JGR Earth Surface

RESEARCH ARTICLE
10.1029/2023JF007105

Special Section:
Controls and Biasing Factors in Sediment Generation, Routing, and Provenance: Models, Methods, and Case Studies

Intra-Seasonal Variability in Sediment Provenance and Transport Processes in the Brahmaputra Basin

Abhishek Dixit[1], Hilmar von Eynatten[2], Jan Schönig[2], Volker Karius[2], Chandan Mahanta[1], and Subashisa Dutta[1]

[1]Department of Civil Engineering, Indian Institute of Technology Guwahati, Guwahati, India, [2]Department of Sedimentology and Environmental Geology, Geoscience Center, University of Göttingen, Göttingen, Germany

Key Points:

- Time-series analysis of sediment composition during two major flooding events of a single monsoon season is presented
- The two flooding events show contrasting grain-size, chemical and mineralogical composition
- Temporal variations in sediment composition pose constraints on the interpretation of provenance and dispersal based on individual samples

Supporting Information:

Supporting Information may be found in the online version of this article.

Correspondence to:

J. Schönig and A. Dixit,
jan.schoenig@uni-goettingen.de;
abhishek.dixit@iitg.ac.in

Citation:

Dixit, A., von Eynatten, H., Schönig, J., Karius, V., Mahanta, C., & Dutta, S. (2023). Intra-seasonal variability in sediment provenance and transport processes in the Brahmaputra basin. *Journal of Geophysical Research: Earth Surface*, *128*, e2023JF007105. https://doi.org/10.1029/2023JF007105

Received 7 FEB 2023
Accepted 12 MAY 2023

Author Contributions:

Conceptualization: Abhishek Dixit, Hilmar von Eynatten, Chandan Mahanta
Formal analysis: Abhishek Dixit, Hilmar von Eynatten, Jan Schönig, Subashisa Dutta
Investigation: Abhishek Dixit, Jan Schönig, Volker Karius

Abstract Sediment composition in modern fluvial settings is commonly assessed regarding spatial but rarely temporal variability, potentially leading to a bias of unknown extent. Here, we present the grain-size distribution, bulk chemical and mineralogical composition of a time-series set of 36 suspended sediment samples from the Brahmaputra river, as well as clay and heavy mineral analysis of selected samples. Sampling covers the June–November 2021 period, which included two major flooding events. We show that the two flooding events are characterized by contrasting grain size, with the first event characterized by a grain-size minimum and the second by a grain-size maximum. Although grain sizes of the first flood and the period after the second are similar, their compositions differ significantly, highlighted by a factor-two decrease of biotite largely compensated by an increase in quartz. By contrast, the content of garnet, clinopyroxene, sillimanite, and rutile increased compared to epidote and amphibole during the second flood event. By relating the results to spatio-temporal rainfall and discharge patterns and basin morphology, we conclude that the first flooding primarily mobilized hydraulically pre-sorted sediments from the exposed sandbars of the floodplains, while those sandbars are already submerged during the second flooding in a single-channel system, resulting in higher sediment contributions from highland tributaries draining igneous and high-grade metamorphic rocks. Such temporal variations pose constraints on the interpretation of compositional differences between individual samples regarding sediment provenance and dispersal and should be considered in studies of modern drainage basins as well as ancient sediment routing systems.

Plain Language Summary Sediment provenance, which refers to where the sediment in a river comes from, is important to understand because it can tell us about the geology of an area, various earth-surface processes and how the landscape is changing over time. However, sediment provenance is typically studied at a spatial scale in present day river basins, and temporal variability is rarely considered. This study examines the physical, chemical and mineralogical properties of sediment in the Brahmaputra river during two major flooding events that occurred in the same season. The results show that the sediment composition varies between the events, indicating a change in the relative proportions of distinct sources. This emphasizes the importance of considering temporal variations in sediment composition when interpreting sediment provenance signals.

1. Introduction

The composition and provenance of sediments in fluvial systems are mainly controlled by the parent lithology as well as physical and chemical processes (e.g., Johnsson, 1993; Weltje & von Eynatten, 2004). These, in turn, are commonly associated with large-scale processes such as regional tectonics (e.g., Dickinson, 1985; Garzanti & Andò, 2007) and/or climate (e.g., Nesbitt et al., 1997; von Eynatten et al., 2016). However, smaller scale spatial and temporal processes like seasonality (Golombek et al., 2021; Jian et al., 2020), mass wasting events (Rai & Singh, 2007) and hydraulic processes (Garzanti et al., 2010, 2011; Lupker et al., 2012) may affect sediment composition and provenance-related interpretation, but are sparsely considered to date. Understanding these small-scale processes and evaluating their influence becomes particularly important when amalgamating data from sediment samples taken at different times and locations.

Intense monsoon and diverse geology of the Brahmaputra basin (Sarma, 2004) provide an excellent natural system to investigate the fluvio-sedimentary response to seasonality and many stochastic events happening at a finer temporal scale. The Brahmaputra river shows an extreme seasonality effect in water discharge. Estimates

Methodology: Abhishek Dixit, Hilmar von Eynatten, Volker Karius
Resources: Hilmar von Eynatten, Chandan Mahanta
Supervision: Hilmar von Eynatten, Chandan Mahanta, Subashisa Dutta
Visualization: Abhishek Dixit, Hilmar von Eynatten, Jan Schönig
Writing – original draft: Abhishek Dixit, Jan Schönig
Writing – review & editing: Abhishek Dixit, Hilmar von Eynatten, Jan Schönig, Volker Karius

show that 87% of the total sediment discharge occurs in the monsoon period (Islam et al., 1999). Previous works have utilized representative monsoon samples for geochemical, mineralogical and other properties with the underlying assumption of homogeneous sediment delivery (Enkelmann et al., 2011; Garzanti et al., 2004; Lupker et al., 2017; S. K. Singh & France-Lanord, 2002). Their provenance mixing models give large uncertainties (up to 27%) in source apportionments (Garzanti et al., 2004; S. K. Singh & France-Lanord, 2002), but the reasons for uncertainties have not been discussed in detail. Temporal variations of the dissolved load in the course of 1 year have been observed previously (Rai & Singh, 2007; Samanta et al., 2019), but similar efforts can also be made for riverine solid matter.

In this study, we examine intra-seasonal variations in chemical and mineralogical sediment composition, which may ultimately have implications for provenance models. These variations are linked to seasonal changes in rainfall and discharge identified by high-frequency time-series analysis coupled with statistical and remote-sensing-based tools. Results suggest temporal changes in relative proportions of sediment sources across different parts of the drainage area.

2. Study Area

2.1. Geology

The Brahmaputra traverses through diverse geological and hydrological environments (Figure 1). The lithology of the geological units is summarized in Table 1 (e.g., Garzanti, 2019; S. K. Singh, 2007). The Brahmaputra flows as Yarlung along the Indus-Yarlung Suture Zone, draining turbidites and ophiolitic mélange in the upper course (Zhu et al., 2013). The lower course and northern tributaries drain the gabbroic to granodioritic batholiths of the Gangdese belt (Wen et al., 2008). A part of the lower Yarlung basin also drains the Precambrian orthogneisses and metasediments of the Lhasa Block (Yin & Harrison, 2000). The local bedrocks south of the Indus-Yarlung Suture Zone comprise the Tethys Himalayan sedimentary (THS) rocks and higher-grade gneisses of the High Himalayan Crystalline (HHC). As the Yarlung reaches the easternmost corner, it enters the Eastern Syntaxis zone, which comprises rapidly exhumed metamorphic rocks of upper amphibolite to granulite facies in its core (Burg et al., 1998). As the river completes its U-turn around the Namcha Barwa—Gyala Peri massif, it continues as Siang. The Siang and other Himalayan tributaries of the Brahmaputra drain the Himalayan geological units, that is, THS rocks, HHC gneisses, schists and marbles intruded with leucogranites, Lesser Himalayan metamorphic rocks (medium to low-grade quartzites, schists), sedimentary rocks (limestone, dolostones and shales) and Neogene molasse of Siwalik group (Garzanti, 2019). Siang also has vesicular to amygdaloidal and porphyritic basalt (Abor Volcanics) in the Lesser Himalaya formation (Acharyya, 2007).

Unlike Himalayan tributaries, a major part of the eastern tributaries (Dibang and Lohit) drain Transhimalayan plutonic rocks in Mishmi Hills, which includes diorite-tonalite-granodiorite complexes and tholeiitic metavolcanic rocks (Gururajan & Choudhuri, 2003; Misra, 2009; Salvi et al., 2020). Dibang and Lohit then cross the Tidding Suture as a continuation of the Indus-Yarlung Suture Zone to enter the Himalayan units.

Where Lohit, Dibang and Siang coalesce upstream of Dibrugarh, these major tributaries enter floodplains and flow as Brahmaputra, forming wide braided channels having numerous lateral and mid-channel sandbars. The floodplain sediments are superimposed on the Precambrian Indian plate basement, which is exposed at some locations in the drainage basin (e.g., Mikir Hills, Shillong Plateau). The southern tributaries (Kopili, Dhansiri, Dihing) drain the Shillong Plateau and Mikir Hills (Figure 1), consisting of gneiss and schist along with pelagic sediments and turbidites associated with Naga-Patkai Hills (Brunnschweiler, 1966; Mitra & Mitra, 2001; Uddin et al., 2007).

2.2. Topography and Hydrology

There exists a contrast in hydrological and climatic zones in the Brahmaputra basin. The Yarlung flows through stable flat topography (1.63 m/km) at an elevation of >4,000 m a.s.l. and lies in the rainfall shadow zone of the Himalayan range. As Yarlung takes the big bend around the Namcha Barwa (7,755 m)-Gyala Peri (7,150 m) massif and later emerges out of the Eastern Syntaxis, its elevation drops sharply over a length of 300 km from ca. 3,000 to ca. 100 m a.s.l. at an average rate of 9.7 m/km. In the floodplains, the slope is gentle and gradually reduces from 0.62 m/km near Pasighat to 0.11 m/km near Guwahati and finally 0.079 m/km in Bengal Delta

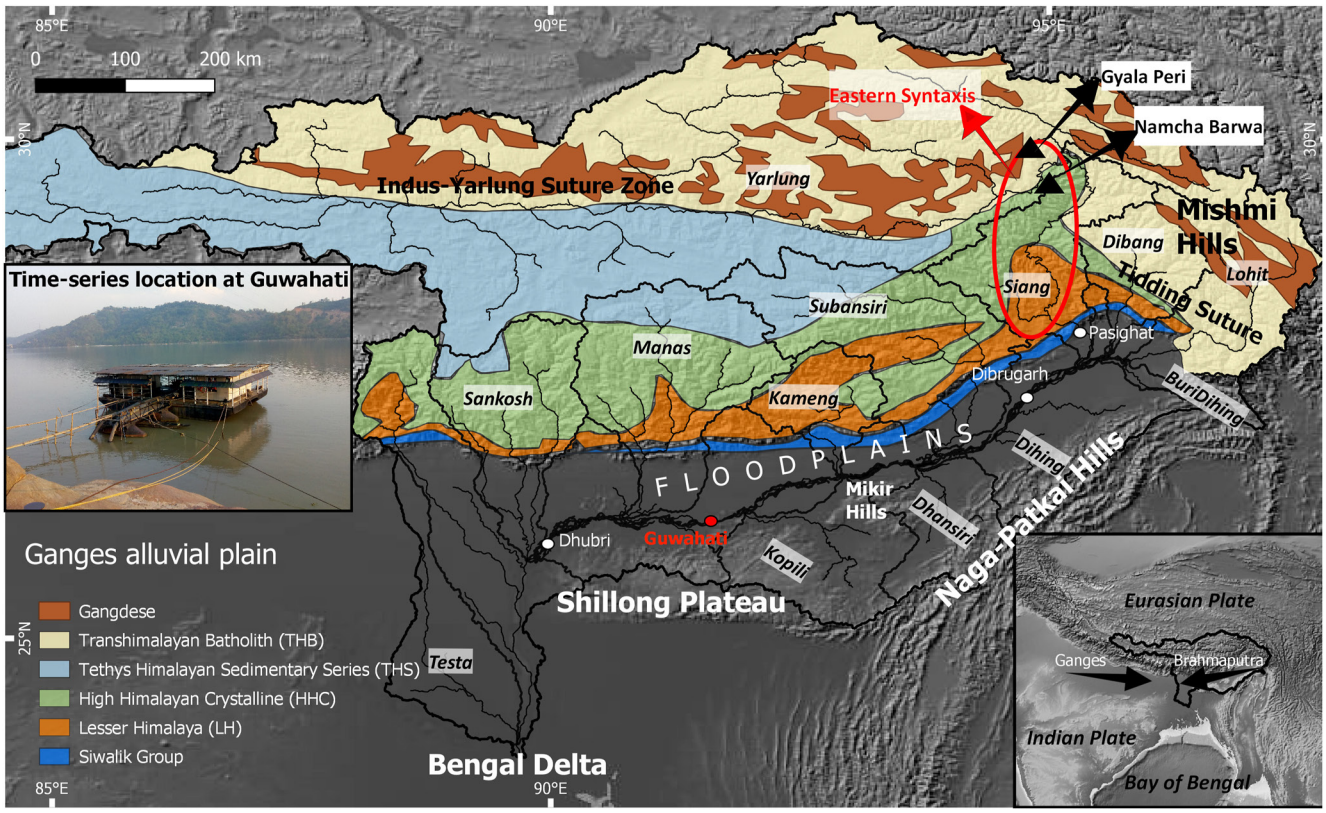

Figure 1. Brahmaputra river network and major geological units. Right inset shows the basin outline on world map. Red dot shows the time series sampling location at Guwahati. Samples were collected from a barge, which was afloat 15–20 m off the bank (left inset).

(Sarma, 2005). The southern tributaries drain an elevation range of around 2,000 to 100 m a.s.l. and have a length of 200–300 m. The eastern tributaries Dibang and Lohit originate at elevations of 5,255 m and 6,614 m a.s.l., respectively (V. Singh et al., 2004).

The Brahmaputra basin experiences extreme seasonality, with 66%–85% of its annual rainfall occurring during the southwest monsoon season from May to October (Sarma, 2005). During peak monsoon from June to August, rainfall may reach up to 500 mm/month, whereas little to no rainfall occurs in the dry period from November to February (S. K. Singh, 2007). Spatially, the upper (near Dibrugarh) and lower (near Dhubri) floodplains receive intense rainfall, whereas the central part (near Guwahati) lies in the rain shadow of the southern hills (Shillong Plateau and Mikir Hills). The annual precipitation is <300 mm in the Yarlung basin, 5,000 mm in Eastern

Table 1
Lithologies of Different Geological Units in the Brahmaputra Basin

Units	Lithology
Transhimalayan Batholith	Ophiolitic mélange (Indus-Yarlung Suture Zone), gabbro to granodiorite (Gangdese), orthogneiss and metasediments (Lhasa Block)
Tethys Himalayan Sedimentary Series	Schists, quartzites, marble, sandstone, shale, chert, limestone
High Himalayan Crystalline	High-grade gneiss, schists, marbles
Lesser Himalaya	Medium to low-grade quartzites, schist, limestone, dolostone, shales
Siwalik Group	Sandstone, conglomerate, siltstone, mudstone (Neogene molasse)
Mishmi Hills	Calc-alkaline diorite-tonalite-granodiorite, tholeiitic metavolcanics, gneiss
Naga-Patkai Hills	Pelagic sediments, turbidites
Shillong Plateau and Mikir Hills	Gneiss, schist

Table 2
Sediment Source Proportions of Various Geological Units at Different Locations Along the Main Brahmaputra Channel

Locations	Yarlung	Eastern syntaxis (Namcha Barwa)[a]	Himalayan tributaries	Mishmi Hills	Shillong Plateau	Naga-Patkai Hills	Study
Pasighat		60%–71%					1
		75%					2
Dibrugarh		81 ± 21%		19%			3
Guwahati		58 ± 23%					3
Dhubri	5%	45 ± 27%	40%	10%			3,4
		41% (35%)	23%	24%	11%	1%	2
	12%	30%	36%	22%		1%	5
BoB[b]		25% (21%)	14%	14%	7%		2

[a]Eastern Syntaxis includes Namcha Barwa gorge, and Siang valley. Numbers in bracket show the contribution from the Namcha barwa gorge. [b]In case of Bay of Bengal (BoB) missing proportion (ca. 40%) is derived from the Ganga basin. 1- Enkelmann et al. (2011), 2- Garzanti et al. (2004), 3- S. K. Singh and France-Lanord (2002), 4- S. K. Singh (2006), 5- Lupker et al. (2017).

Syntaxis, 1,000–2,000 mm on the southern slopes of Himalaya and 3,000 mm in Mishmi Hills. Naga-Patkai and the Shillong Plateau receive heavy rainfall of 4,000 mm/year, but these areas do not drain entirely toward the Brahmaputra basin (S. K. Singh, 2007).

The water discharge also shows strong inter- and intra-season variability resulting in dynamic morphology of the floodplains (Nandi, Pradhan, Dutta, & Khatua, 2022; Nandi, Pradhan, Padhee, et al., 2022). The monthly water discharge at Guwahati is 40,000 m^3/s in monsoon and 5,000 m^3/s in the dry season (for 1956–1979, Data: Global Runoff Data Center, www.compositerunoff.sr.unh.edu). About 80% of the water flows during the monsoon months only. The major source of water is monsoon rainfall, but glaciers and groundwater also contribute (Immerzeel et al., 2010; Kaser et al., 2010). Multiple discharge peaks are common in the Brahmaputra main trunk and are related to snowmelt and rainfall in different parts of the basin (Karmaker & Dutta, 2010). Spatially, Siang is the major contributor of the water discharge (32%) and all other tributaries contribute 1%–10% each (Sarma, 2005).

2.3. Sediment Flux, Sources, and Generation Processes

The Brahmaputra is a sediment-laden river. The directly gauged annual sediment flux at the Bengal Delta is 400–700 × 10^6 t (Goswami, 1985; Islam et al., 1999; Milliman & Farnsworth, 2011) and ca. 10 × 10^6 t at Yarlung basin outlet (Shi et al., 2018). However, this figure might be largely underestimated, and the total actual sediment flux of the entire basin might be up to 1 × 10^9 t if bedload is incorporated (Galy & France-Lanord, 2001). Almost 87% of sediments are transported in the monsoon months when the sediment concentration may reach up to 2,000 mg/l. In the dry period, it can be as low as 100 mg/l (Islam et al., 1999). Estimated sediment proportions from various sub-drainages of the Brahmaputra basin are given in Table 2. Eastern Syntaxis dominates the sediment load at floodplains, ranging from ca. 60%–80% at Pasighat, Dibrugarh and Guwahati, with little dilution from northern, eastern and southern tributaries. At the Eastern Syntaxis, sharp gradients coincide with high precipitation (Finnegan et al., 2008; Salvi et al., 2017) which trigger massive landslides (Larsen & Montgomery, 2012), occasionally amplified by glacier lake outburst floods (Lang et al., 2013; Panda et al., 2020; Turzewski et al., 2020), making it one of the highest sediment yielding locations in the world (Milliman & Farnsworth, 2011). The sediment generation processes are multiple and include landslides, glacier/landslide outburst floods, river incision, river widening, channel relocation and sheet/rill erosion, whereby landslides are considered as the largest contributor (Wasson et al., 2022). The contribution of the Eastern Syntaxis decreases downstream to values of ca. 30%–45% at Dhubri and ca. 25% at the delta.

3. Material and Methods

3.1. Sampling

Time-series samples were collected at Guwahati from a stable barge floating ca. 15–20 m off the north bank of the river (left inset of Figure 1). Additionally, midstream samples were collected by boat when the logistics

and flow conditions were favorable. Sampling covered major monsoon flooding events from 29 June 2021 to 07 November 2021. Every month has one midstream sample, except August. The frequency of the sampling is one to 10 days. During high flow, sampling frequency was increased to capture the peak discharge sediments. A large carboy (10 l) was used to collect the water from the top water surface. Under low flow conditions, up to 50 l of water was collected. The carboys were kept undisturbed for several days after collection. After siphoning out the clear supernatant water, settled solids were extracted. An aliquot of 500 ml of water was collected to determine the sediment concentration, calculated by dry weighing before and after filtration through 0.45 µm cellulose nitrate filters. Extracted sediment samples were stored dry and analyzed at the University of Göttingen (Geosciences Center, Department of Sedimentology and Environmental Geology).

3.2. Grain-Size Analysis

Dried samples were tip-sonicated for 30 s with a supersonic device before analysis. Grain-size distribution was determined using a Beckman and Coulter Type LS13320 laser particle size analyzer with a polarized intensity differential scattering system (PIDS). Results are expressed in volume % over the measured grain-size range of 0.04–2,000 µm. Grain sizes were computed using an optical model for Quartz (R.I. 1.556/0.1).

3.3. Bulk and Clay XRD

Bulk X-ray diffraction (XRD) was performed on samples to identify and quantify mineral phases. Samples were admixed with 10% ZnO as internal standard. The mixture was wet milled with a McCrone mill in ethanol and dried at 60°C. Dried samples were disaggregated and pulverized in a vibration mill (Pulverisette 23, Fritsch) before preparing the randomly oriented mounts in backloading cuvettes. Bulk XRD was performed using an Orion Comet P2 Powder Diffractometer by Eigenmann GmbH. Quantitative analysis was performed by Rietveld refinement using the Profex software (Doebelin & Kleeberg, 2015).

For clay mineralogy, XRD scans were obtained on oriented mounts of the clay-sized particles (<2 µm fraction). Samples were treated with hydrogen peroxide and sodium dithionite for organic matter and iron removal, respectively. Treated samples were centrifuged multiple times to obtain <2 µm fraction, and oriented mounts were prepared and air-dried on a porous plate.

The relative percentages of illite, kaolinite and chlorite were determined using weighting of integrated peak areas of the characteristic basal reflections with empirical factors (Biscay, 1965). For illite, the characteristic peak area of 10 Å was multiplied by 4, and the summed kaolinite and chlorite intensity peak area of 7 Å was multiplied by 2. The relative proportions of kaolinite and chlorite were obtained using the peak-intensity ratio of 3.57 to 3.54 Å. Since the Brahmaputra sediments are reported to have a negligible amount of smectite (Khan et al., 2019), ethylene-glycol solvation was not performed on oriented mounts. The objective of the clay mineralogy was to observe any stark change in the clay fractions. Neglecting smectite may have introduced minor amount of overestimation of the illite, chlorite and kaolinite proportions, but does not change the general interpretation of the study.

3.4. Chemical Analysis

Chemical analysis on bulk samples was performed using an Agilent 5,100 Inductively Coupled Plasma—Optical Emission spectrometer (ICP-OES). Sample amounts of 0.1 mg were dried overnight and treated with 2 ml HNO_3 (65 wt%) in Teflon beakers at room temperature to remove carbonates. After that, samples were treated with a solution of 3 ml HF (40 wt%) and 3 ml $HClO_4$ (70 wt%) in pressurized Teflon beakers at a temperature of 150°C in Picotrace DAS 30 digestion assembly for 12 hr. Afterward, an evaporation step at 180°C for 12 hr and another pressure phase at 150°C for 2 hr followed, dissolving the residues with 0.5 ml HCl and 2 ml HNO_3. The resulting liquid was diluted to a total of 100 ml by Milli-Q water and analyzed by ICP-OES. The reported elements have a precision in the range of 0.5%–5% relative standard deviation and accuracy of less than 10% for all elements except Y and Pb, which show accuracies of 20% and 11%, respectively, determined for the JA-2, JG-2 reference material (Imai et al., 1995) and Pb-soll (Pikrite, in-house standard).

3.5. Semi-Automated Heavy Mineral Analysis by Raman Spectroscopy

Heavy mineral analysis was performed on three samples (29/06/21, 16/08/21, and 30/08/21), selected depending on the grain size, sampling date, and availability of sufficient sample material. Samples were treated with 10% acetic acid to remove the carbonates and two grain-size fractions, 10–30 µm and 30–62 µm, were separated by

wet sieving using nylon sieves. Together, these fractions represent ca. 48% of the total sample. The heavy-mineral fraction was concentrated by centrifugation in Na-Polytungstate with a density of ca. 2.87 g/cm^3. The separated heavy mineral fractions were recovered after partial freezing with liquid nitrogen (see Andò (2020) for detailed separation description). Since during a preliminary investigation, organic matter occurring at grain surfaces as well as in small cracks and cleavage planes has been observed to strongly bias the quality of the Raman spectra, organic matter has been removed in four steps by treatment with n-hexane, dichloromethane(DCM)/methanol (2:1), DCM/methanol (3:1) and pure DCM. The heavy mineral concentrates were embedded in synthetic mounts using a bonding epoxy. Mounts were grounded with silicon carbide abrasive paper and polished in three steps with Al_2O_3 abrasives in water suspension up to the finest step with a particle size of 0.05 µm.

Mineral identification and quantification were performed using semi-automated heavy-mineral analysis by Raman spectroscopy after Lünsdorf et al. (2019): (a) Sample mounts were photographed in reflected and transmitted light using a Zeiss AxioImager M2m microscope with an automated *x-y-z* stage and a 20× objective with a numerical aperture of 0.45; (b) individual photographed tiles were stitched to a single image containing *x-y-z* information for each pixel; (c) reference and measurement points were defined in the "Coordsetter" software by applying the ribbon-counting method (Mange & Maurer, 1992); (d) the resulting coordinate list was transferred to a Horiba Jobin Yvon XploRA Plus spectrometer equipped with an Olympus BX41 microscope and a motorized *x-y-z* stage; (e) one spectrum was acquired for each defined point as well as a 4-Acetamidophenol standard bracketing every 100 analyses. Measurement conditions include a circularly polarized laser with a wavelength of 532 nm and a maximal output power of 100 mW, a confocal hole diameter and slit set to 100 µm, a 100× long-working-distance objective with a numerical aperture of 0.80, a 1,200 li/mm grating covering a spectral range of 100–2,800 cm^{-1} with a spectral resolution of ca. 3.1 cm^{-1}, a laser power filtered to 10% for grains showing a transmitted light gray value ≥50% and 1% for those <50 (darkest ca. 20%) and an automated exposure time estimated to reach 5,000 counts for each individual analysis but limited to a maximum of 60 s per spectrum.

Following Lünsdorf et al. (2019), the resulting spectra were automatically corrected for a temporal drift based on characteristic Raman band positions of the 4-Acetamidophenol standard, the background was removed based on spectrum convolution and a Hanning window, the signal-to-noise ratio (SNR) for each spectrum was estimated and those spectra showing a SNR ≤10 were excluded, while those showing a SNR >10 were smoothed, scaled, corrected for the epoxy embedding medium spectrum and compared to a modified version of the RRUFF database (Lafuente et al., 2015). A hit index (HI; Rodriguez et al., 2011) was assigned to each pair of analyses and reference spectra, which was empirically categorized into "good hit" (HI < 0.15), medium hit (HI 0.15–0.30) and no hit (HI > 0.30). Mineral identification for spectra assigned to the "good hit" category was directly accepted, those in the "medium hit" category were re-examined for potential misclassifications and mixed spectra, and those of the "no hit" category were screened for occasional spectra that still show characteristic Raman bands enabling unequivocal mineral identification. All grains that could not be assigned to a specific mineral but show a transmitted light value similar to or lower than opaque minerals within the sample, such as ilmenite and magnetite, are grouped as "opaque." All remaining analyses are evaluated as "not identified."

3.6. Satellite Data and Products

Rainfall data are presented in 5-day time steps and at a spatial resolution of 0.05° obtained through Climate Hazards Group InfraRed Precipitation with Station (CHIRPS) data (Funk et al., 2015). Discharge data was obtained from the Global Flood Monitoring System, which uses real-time Tropical Rainfall Measuring Mission Multi-satellite Precipitation Analysis and Integrated Multi-Satellite Retrievals for Global Precipitation Measurement precipitation information as input to a quasi-global (50°N–50°S) hydrological runoff and routing model running on a 1/8th degree latitude/longitude grid (Wu et al., 2014). Optical satellite images show a spatial resolution of 10 m and have been acquired for green, red and near infrared bands by Sentinel-2: Multi Spectral Instrument, Level-2A data.

4. Results

4.1. Grain-Size Distribution and Variability

Samples are predominantly in the silt range with a minor amount (ca. < 25%) of total clay and very-fine to fine sand (Figure 2). They show a two-fold variability in the grain-size statistics, with median grain size varying between 8 and 21 µm and means between 15 and 35 µm. Since the grain-size distribution patterns remain consistent during the study period, the different grain-size parameters show rather similar variability patterns. For

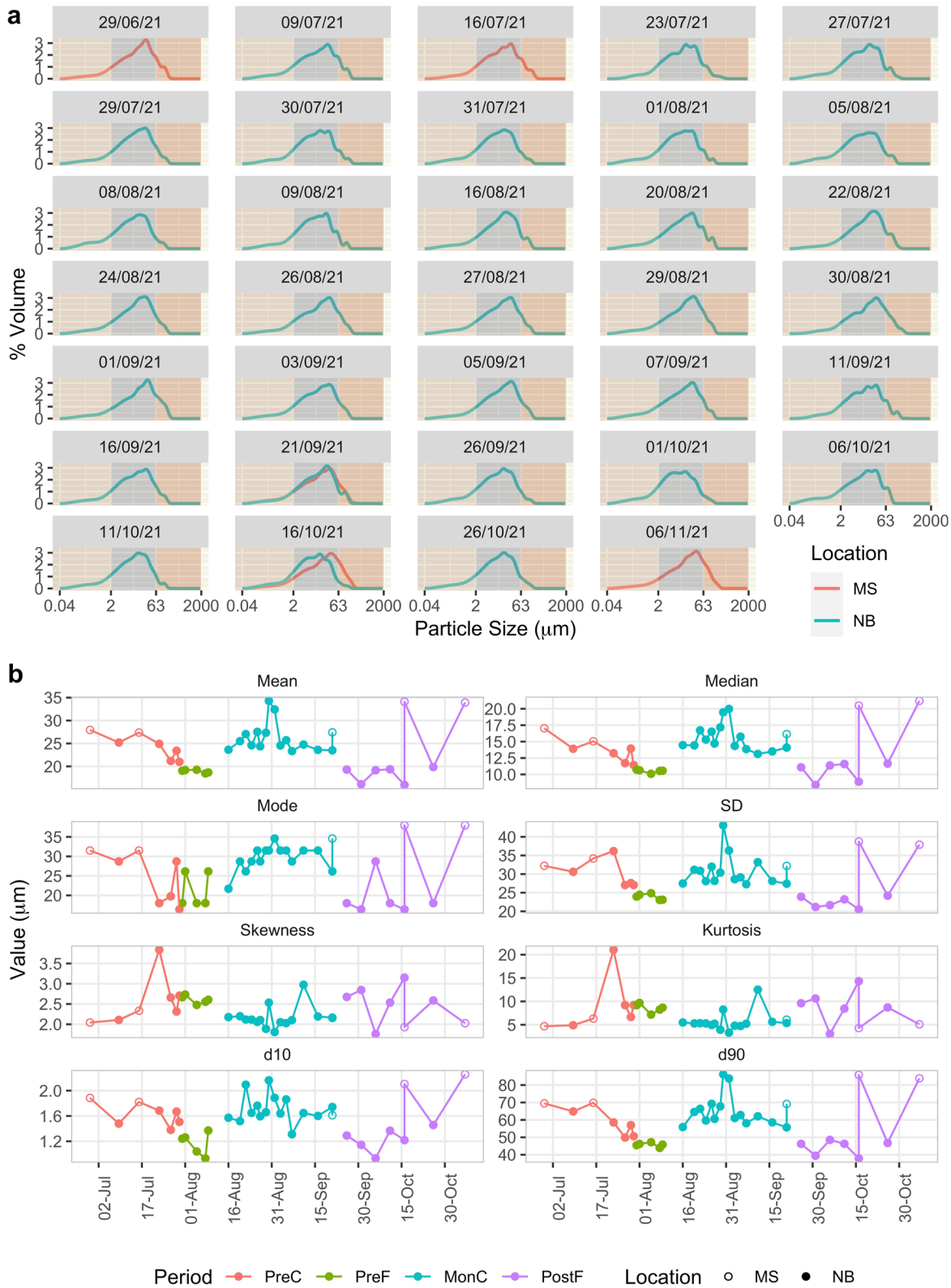

Figure 2. Grain-size distribution (a) and Grain size statistics (b). NB = near bank, MS = midstream. Color coded periods are described in text.

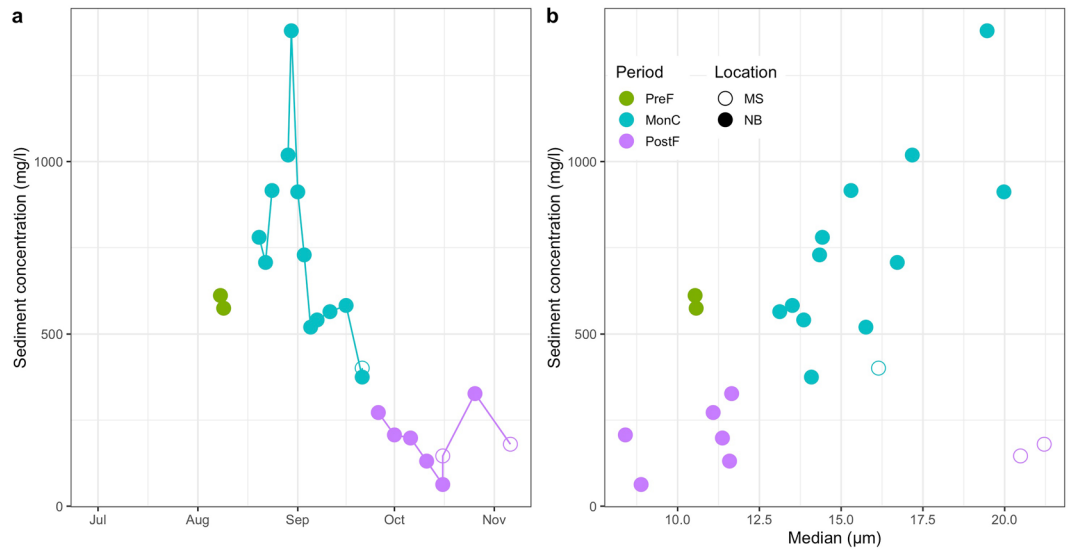

Figure 3. (a) Sediment concentration variation in PreF, MonC, and PostF periods (b) Cross-plot of sediment concentration and grain size. See the caption of Figure 2 for legend description.

instance, d10 and d90 also show a two-fold variability from 1 to 2.2 μm and 37 to 86 μm, respectively. Samples are invariably poorly to very poorly sorted, mesokurtic and fine skewed.

Based on grain-size variation, the study period is divided into four time periods (Figure 2b). Though this subdivision is subjective, it reflects a general trend. The "Pre Coarse" (PreC, red) period is from 29 June 2021 to 30 July 2021, when the grain size is relatively coarse before it decreases in the "Pre Fine" (PreF, green) period from 31 July 2021 to 09 August 2021. The grain size shows a maximum at the end of August in the "Monsoon Coarse" (MonC, blue) period from 16 August 2021 to 21 September 2021. Afterward, the grain size decreases to the levels of PreF in the "Post Fine" (PostF, violet) period from 26 September 2021 to 06 November 2021, with notable exceptions of midstream samples on 16 October 2021 and 06 November 2021.

On 2 days (21 September and 16 October), samples were collected from both the midstream and the near bank. Intraday variability in these 2 days can be explained by the flow conditions. Midstream flow conditions are more turbulent than near bank flow conditions (Karmaker et al., 2010; Lupker et al., 2011), which may increase the grain size in the midstream. However, the fact that the grain-size difference on intraday samples of 16 October is higher than that of 21 September does point to the possibility of higher turbulence and mixing across the channel during the MonC period (21 September) compared to the PostF period (16 October). This also suggests that near bank samples during the monsoon (high discharge period) may be considered representative samples of the river.

4.2. Sediment Concentration

The sediment concentration was measured for samples collected after 05 August 2021. The maximum sediment concentration of 1,380 mg/l was observed at the end of August (Figure 3a), correlating with the observed high median grain size (Figure 3b). The minimum concentration (63 mg/l) was observed in the PostF period. Midstream samples have slightly higher concentrations than the near bank samples on 21 September and 16 October (Figure 3). The lesser difference in sediment concentration on 16 September between midstream and near bank is consistent with the grain-size data and suggests higher mixing across the channel in MonC samples than in PostF. Even though the difference in grain size of PreF and PostF samples is less pronounced, the difference in sediment concentration is apparent, with the former having a higher concentration (ca. 600 mg/l) than the latter (ca. 100–300 mg/l). Note that the midstream samples from PostF are significantly coarser than the near bank samples, although sediment concentration is similar (Figure 3b).

4.3. Chemical Data and Covariance Structure

The variability of major and minor elements during the study period is illustrated in Figures 4 and 5 and Figure S1. Grain-size-related elemental variability is evident in all periods. Elements typically enriched in sheet

silicates (Al, K, Mg, Fe, Ti and trace elements Co, Sc, V, Ni, Ga, Li, Cu) show a higher concentration in the finer grain-size samples of the PreF period and are lowest in the coarser grain-size samples of the MonC period. Interestingly, the PostF period does not show enrichment of the same extent of these elements, except for Al, Mn, and Zn, even though the grain size is similar to the PreF period.

Ca, Na, and Sr have higher values in midstream samples consistent with the larger grain size. By contrast, K and Ba show among the lowest concentrations in the midstream samples. This is demonstrated in the biplot (Figure 5a), where midstream samples cluster in the third quadrant, characterized by negative values on PC1 and PC2 reflecting the enrichment of Ca, Sr, and Na. The strong contrast of these elements compared to K, which is associated with Al and LOI, indicates that K is primarily hosted in sheet silicates (not K-feldspar) and Ca, Na primarily in plagioclase feldspar.

Covariance structure highlights grain-size control associated with PC1, explaining ca. 42.09% of total variability and is characterized by positive loadings of Al, K, Fe, Ti, LOI, Ga, Sc, Ni, and Mg (Figures 5a and 5c). All four periods (PreC, PreF, MonC, and PostF) are separated along PC1, with the highest values for the PreF samples and negative values for MonC samples. PC2 explains ca. 26.86% of the variability and is characterized by positive loadings of typically felsic elements like La, Ce, Ba, and Y and negative loadings of typically mafic elements Ca, Ni, Mg, Sr, Na, and P (Figures 5a and 5b). PC3 explains 15.31% of total variability and is mainly characterized by strong negative loadings for the Mn, Pb, and LOI and is thus likely related to clay minerals and organic matter.

4.4. Bulk and Clay Mineralogy

Bulk mineral assemblage majorly consists of quartz, feldspar, mica and clay minerals (Figure 6). Minor peaks of hornblende and diopside (<4%) are also identified in XRD scans. Rietveld refinement may provide variable phase quantities in such complex multiphase assemblages (including weathered minerals) as some of the structural phase models used may not properly reflect the natural mineral structures (e.g., von Eynatten et al., 2016). This may cause noise in the time series pattern, especially if the natural variability is in the range of the refinement uncertainty. Quartz and biotite contents, however, exhibit distinct contrasts between the groups and remain relatively stable even when trying different structural models for the minor phases. Thus, the confidence level for these two phases is high and their concentrations are preferentially used for interpretation in conjunction with other data sets presented in this study.

The proportions of quartz and biotite vary from 21% to 31% and from 5% to 12%, respectively (Figure 6a). In agreement with the chemical data, plagioclase (sum of albite and anorthite: 15%–25%) prevails over K-feldspar (6%–9%). Quartz and biotite show an inverse relation with each other (Figure 6c). The quartz proportions are lowest in PreF period when biotite is highest with up to 12%. Notably, biotite is comparatively low (6%) and quartz is higher in the PostF period, although the grain size is similar to the PreF period. This behavior is consistent with the chemical data (comparatively low K, Fe, and Mg concentrations in PostF). An increase in quartz content within the peak MonC period compared to most other samples is also observed along with increasing grain size. Notably, the PostF period shows a minor decrease in quartz compared to the MonC period, even though the grain-size contrast between the two periods is apparent (cf. Figure 2). This suggests the possibility of a change in provenance in the MonC and PostF compared to previous periods.

The clay mineral proportion in the <2 μm size fraction indicates the dominance of illite over chlorite and kaolinite (Figure 6b). The illite to chlorite ratio differs in bulk and <2 μm fractions. This is probably because the <2 μm fraction does not necessarily contain only the clay minerals. Some other sheet silicates (e.g., biotite, muscovite) can also be present and may contribute to the 10 Å peak from which the illite content is determined. Nevertheless, the main objective of clay mineralogy was to examine the intersample variability within the <2 μm fraction samples to observe any stark changes in kaolinite concentration. An almost uniform clay mineral proportion and low kaolinite concentration (ca. 9%) indicate low and uniform chemical weathering intensity on the temporal scale. The results agree with Khan et al. (2019), who reported similar clay mineral proportions (77% illite, 10% kaolinite, 11% chlorite, and 2% smectite) in the bed sediments of the Bengal Delta.

4.5. Heavy-Mineral Analysis

The heavy-mineral suites, as shown in Figure 7, are characterized by amphibole (32%–41%), epidote-group minerals (24%–33%) and subordinate amounts of clinopyroxene (6%–11%), titanite (7%–9%) and garnet (4%–6%). Minor amounts of apatite, olivine, sillimanite, rutile, tourmaline, orthopyroxene and zircon are observed. The

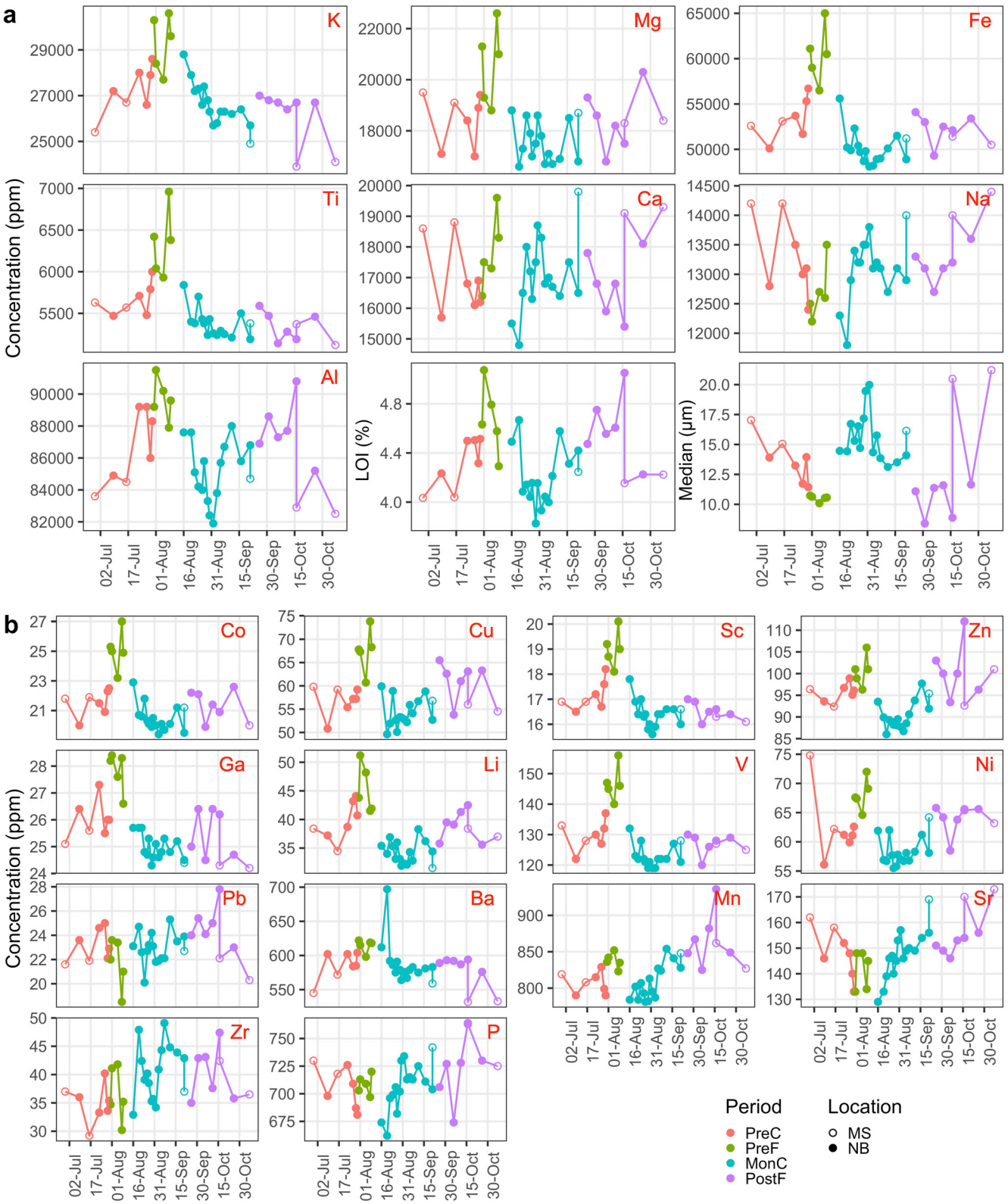

Figure 4. Major (a) and trace (b) element concentrations during the study period. See the caption of Figure 2 for legend description.

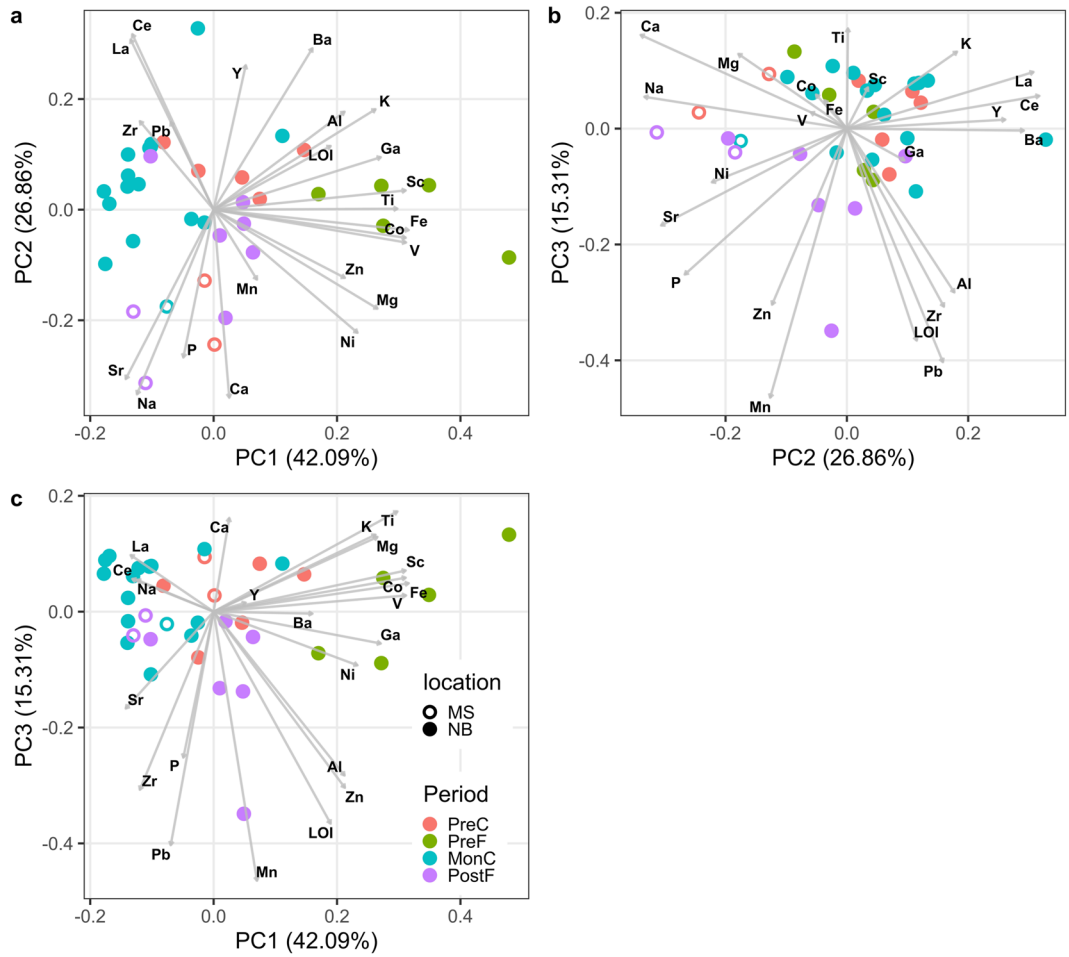

Figure 5. Covariance structure of geochemical data based on the first three principal components (PC1, PC2, PC3) explaining 42.09%, 26.86%, and 15.31% of total variability, respectively. See the caption of Figure 2 for legend description.

heavy-mineral composition remains largely constant across samples and grain-size fractions. However, it is notable that the composition of the peak monsoon sample (30 August) is different from the previous samples (29 June and 16 August), with the former having fewer epidote-group minerals, more pyroxene (almost entirely augitic-diopsidic clinopyroxene) and garnet. This pattern is consistent in both grain-size fractions. In addition, we can consider the composition of clinopyroxene and epidote to be largely unaffected by hydrodynamic effects since they have similar densities of approximately 3.4 g/cm^3.

Figure 7 also displays the heavy-mineral composition of various sub-basins and locations within the Brahmaputra basin. The Yarlung, Siang (Pasighat), Lohit, and Dibang sub-basins have a heavy-mineral suite dominated by amphibole and epidote, whereas the northern tributaries (Subansiri and Manas) are dominated by garnet, amphibole and high-grade minerals (kyanite, sillimanite, andalusite, staurolite). The northern tributaries tend to dilute the upstream signature along the main trunk of the Brahmaputra, particularly increasing the garnet content (at least in the coarser fractions).

4.6. Rainfall, Discharge and Morphological Variability

The floodplains, southern tributaries, and Himalayan and Mishmi foothills received most of the rainfall (Figure 8). A maximum of 285 mm pentad (5 days) rainfall was observed in downstream locations of Siang and eastern basins (Dibang and Lohit). The central part of the floodplains and Yarlung received less rainfall due to falling in the rainfall shadow of the southern hills and Himalayan range, respectively. Temporally, rainfall in June was moderate (57–170 mm). Significant rainfall occurred toward the end of July and end of August. July-end rainfall

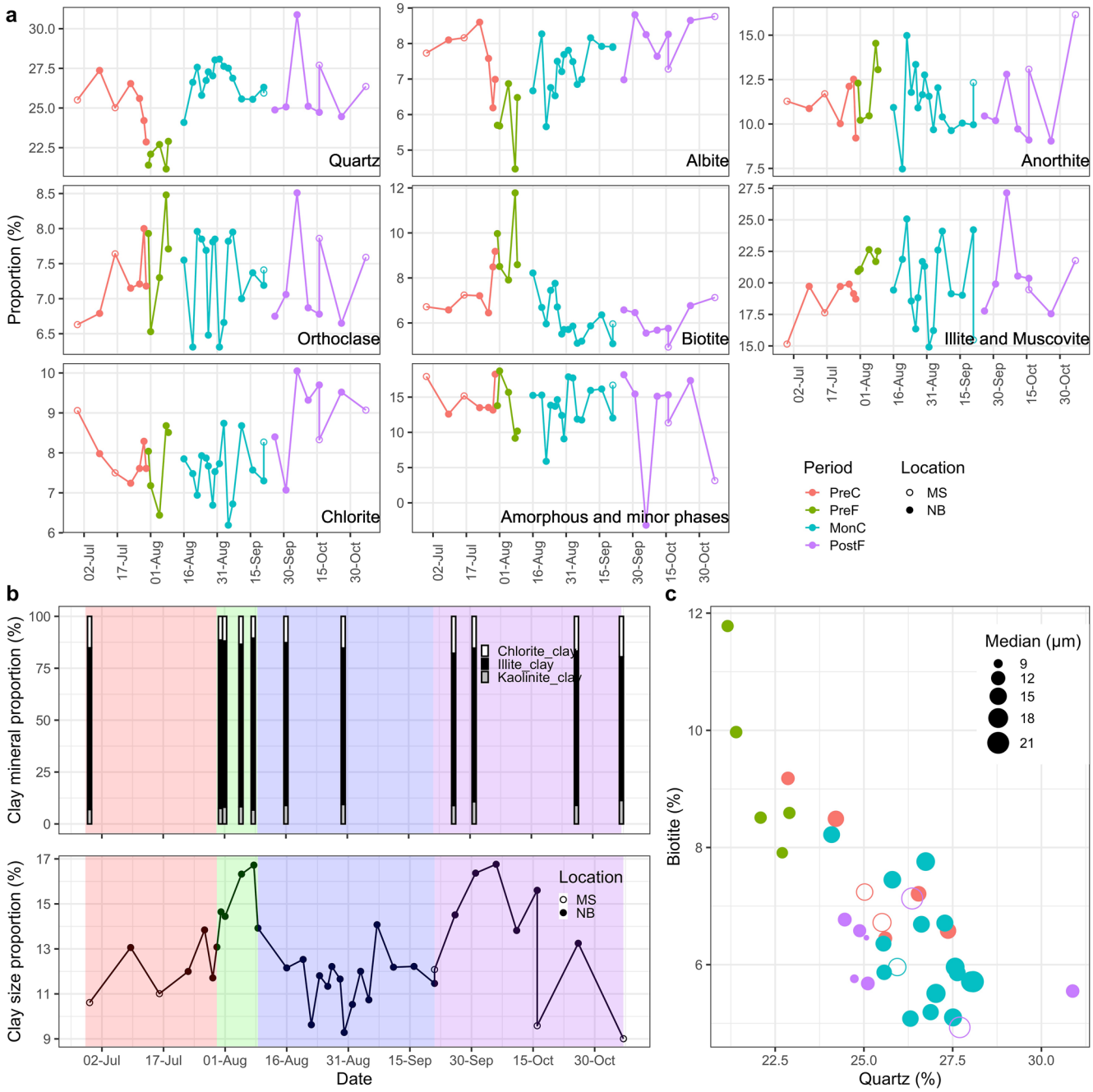

Figure 6. (a) Bulk mineralogy (b) Proportions of clay content (<2 μm). Colors in plot background represent the four defined periods PreC, PreF, MonC, and PostF (left to right). (c) Quartz versus biotite content highlighting their inverse relation. Symbol size refers to grain size. Color and open/filled symbols are according to the previous figures.

was widespread in floodplains and in all tributaries but more concentrated on the eastern and western sides of the basin, whereas August-end rainfall was mainly concentrated in the eastern part. Floodplains did not receive much rainfall in August.

Discharge at Guwahati varied from 2,500 to 17,500 m^3/s with two discharge peaks at July-end and August-end (Figure 9). Out of the major tributaries, Yarlung-Siang is the major contributor to water discharge in the main trunk. Intense rainfall in July-end and August-end coincide with two major discharge peaks at Guwahati. At Dibrugarh, the discharge also has two peaks at the same time. It is noteworthy that the difference of the

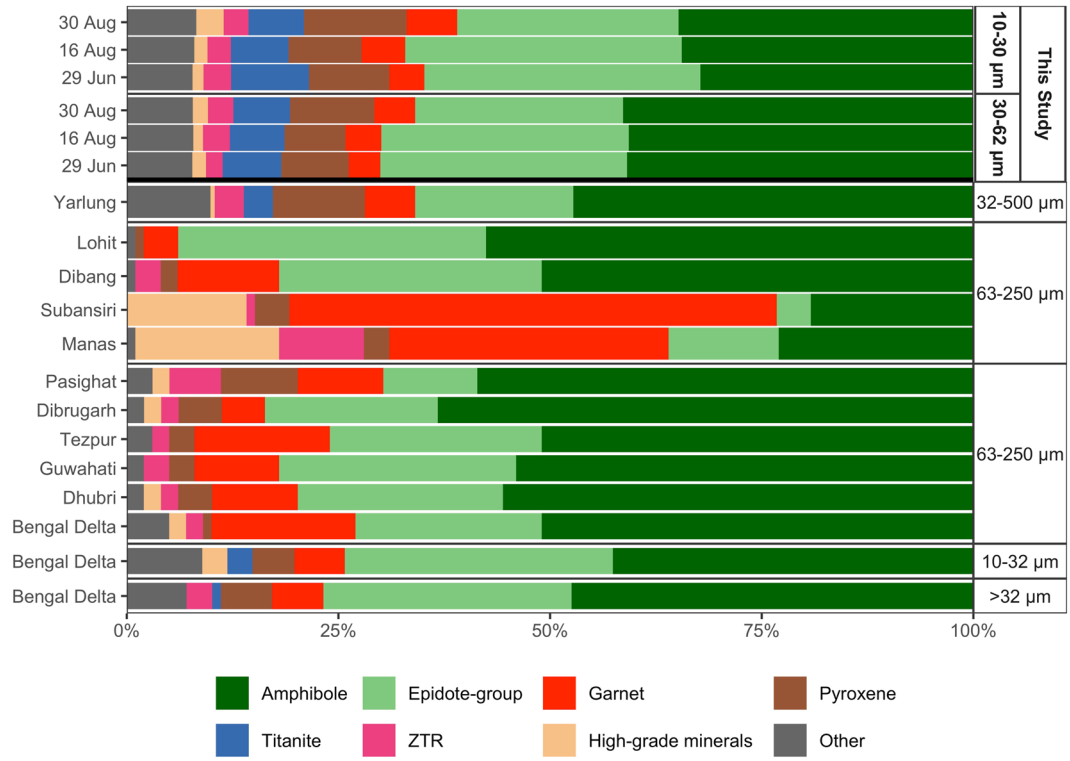

Figure 7. Heavy-mineral suites of samples from this study (29 June, 16 August, 30 August) and of different locations within the basin from secondary sources. The data for the Yarlung location, located just before the Namcha Barwa massif, were taken from Liang et al. (2022). Additional data for other locations were obtained from Garzanti et al. (2004) and Garzanti et al. (2011). ZTR = zircon + tourmaline + rutile, High-grade minerals = kyanite + sillimanite + andalusite + staurolite.

two discharge intensity peaks is different in Guwahati and Dibrugarh. August-end discharge at Dibrugarh is more intense than that of July-end, whereas at Guwahati, July-end and August-end discharge peaks are comparable. This might be explained by the widespread rainfall in the floodplains during July-end, which accumulated the water discharge at the downstream location (Guwahati). In contrast, upstream location (Dibrugarh) did not receive much water from floodplains rainfall in July-end. Instead, concentrated August-end rainfall upstream of Dibrugarh resulted in a higher discharge peak.

Morphological variability of the river was observed for the 140 km river stretch between two morphologically stable nodal points, Tezpur and Guwahati (Nandi, Pradhan, Dutta, & Khatua, 2022). The river exhibits a braiding pattern having vegetated (red) and unvegetated (cyan) sandbars separated by numerous channels, as shown in the 01/05/2021 image of Figure 10. The unvegetated parts of the sandbars are mostly submerged by 25/06/2021, after the minor flood wave of mid-June. Even though the discharge increased till 20/07/2021, there is no visible change in the exposed vegetated sandbar area. Vegetated sandbars are partially covered on 03/09/2021, resulting from the fresh flood wave at the end of August to early September (Figures 8 and 9). Sandbars reappear on 28/10/2021 as the flood recedes in PostF period.

4.7. Earthquake and Mass-Wasting Events

Earthquake and mass-wasting events are common in the Namcha Barwa Gyala Peri region, with recent studies identifying landslides and glacier/landslide lake outburst floods as major processes of sediment generation (Wasson et al., 2022). The Sendongpu glacier on the western flank of Gyala Peri (Figure 11a) has experienced a series of glacier-rock avalanches and debris flows over the past 7 years (Kääb & Girod, 2022; Kääb et al., 2021; Zhao et al., 2022). The most recent mass-wasting event, which occurred on 22 March 2021, generated a massive volume of material, approximately 100×10^6 t (50×10^6 m^3) (Figure 11b, pre-event and Figure 11c, post-event). For comparison, the annual sediment load of Brahmaputra is 520×10^6 t (Milliman & Farnsworth, 2011). Although this event occurred outside the sampling period, it could have potentially modified sediment provenance during

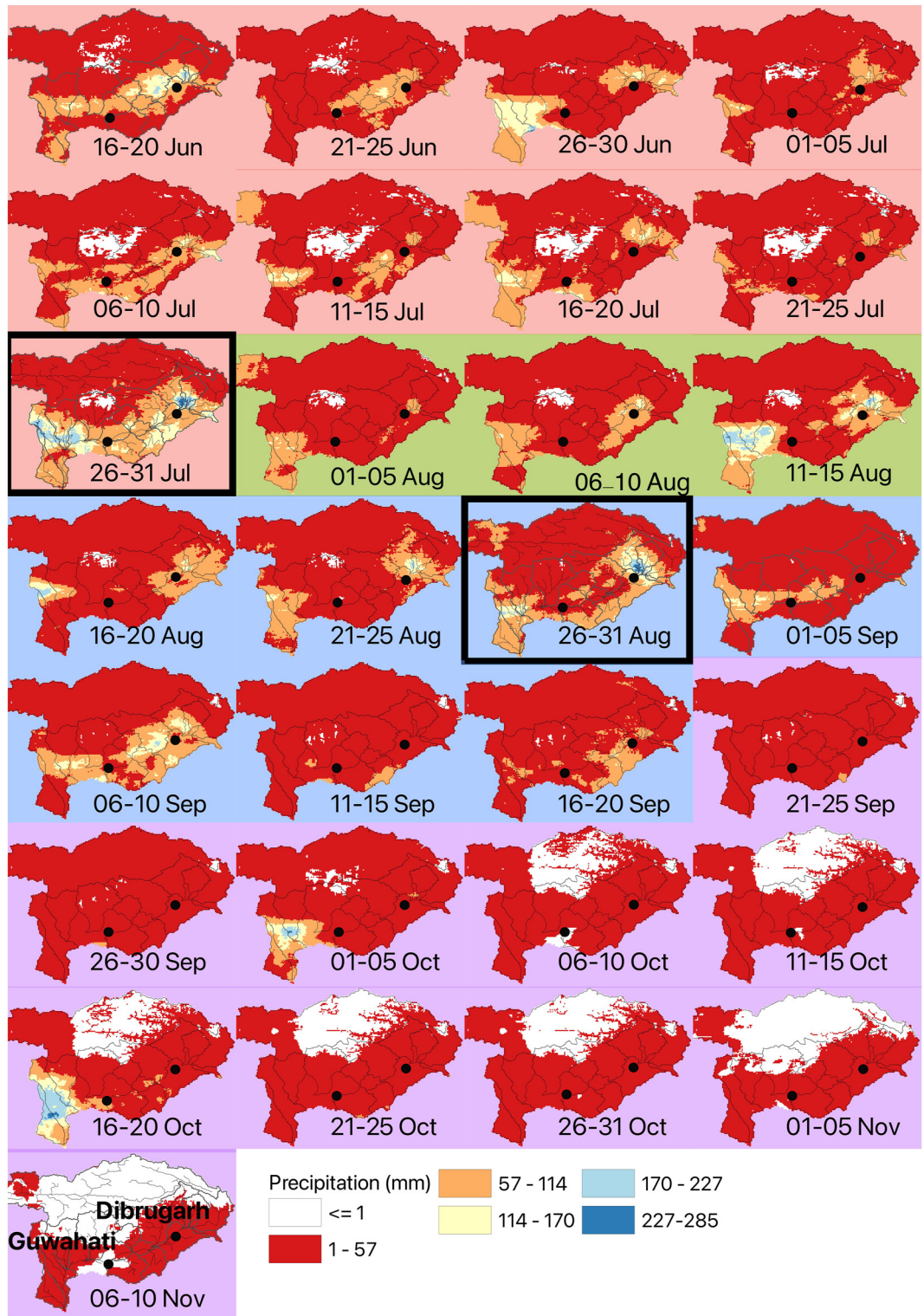

Figure 8. Spatial distribution of total precipitation in pentad (5-days) time step over Brahmaputra basin. Last pentad of the months is of 5 or 6 days. Map background is color coded as periods described in text, that is, PreC (red), PreF (green), MonC (blue), PostF (purple). Black dots indicate the locations at Guwahati (west) and Dibrugarh (east). The black rectangular boxes highlight intense rainfall periods, which coincide with two discharge peaks (cf. Figure 9) and grain-size minimum (PreF) and maximum (MonC) (cf. Figure 2).

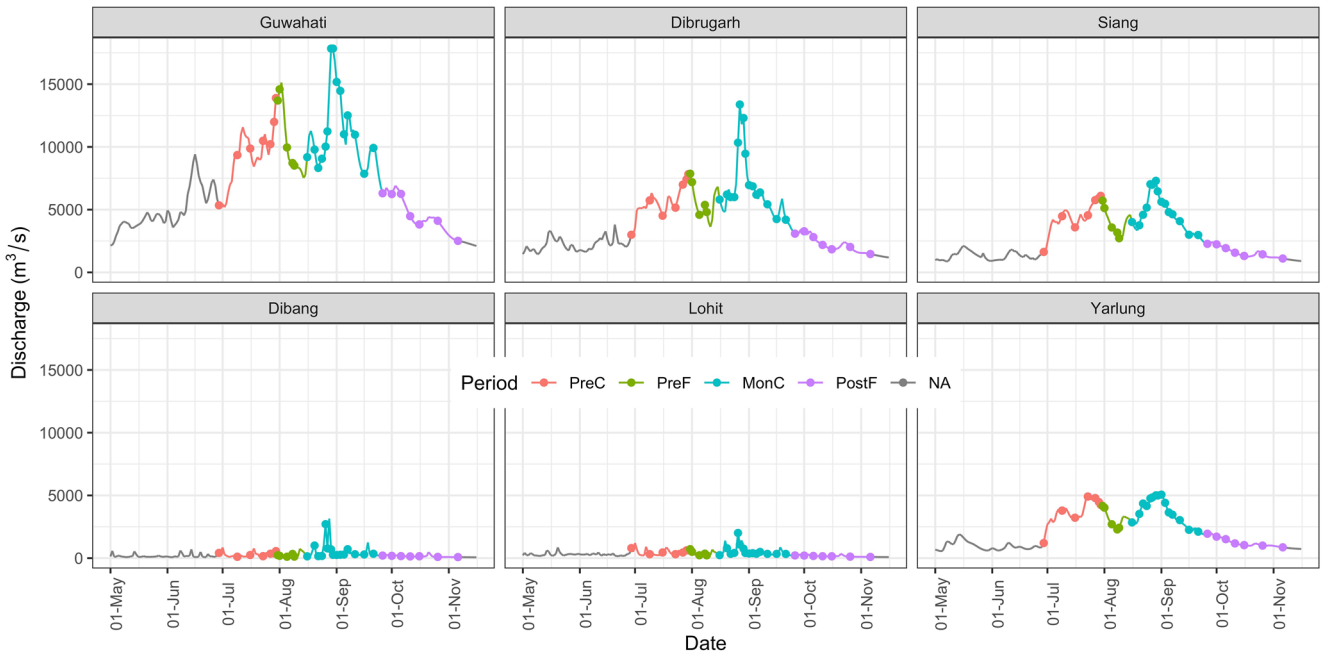

Figure 9. Daily discharge time series (line) at various locations in the Brahmaputra basin. Dots on the discharge curve represent the dates on which sediment samples were collected at Guwahati. Guwahati and Dibrugarh are locations on the main trunk of the Brahmaputra. For Siang, Dibang, and Lohit, locations are the outlet points of these tributaries before they join the main trunk. The location of Yarlung is near Namcha Barwa—Gyala Peri massif (Figure 1).

the upcoming monsoon. Furthermore, an earthquake of M4.2 intensity occurred approximately 30 km away from the Sendongpu valley on 9 August 2021, roughly coeval with the change from the PreF to the MonC period, highlighting the region's high tectonic and morphological activity.

The mass-wasting event caused a temporary partial blockage of the Yarlung river (Figure 11d, pre-event and Figure 11e, post-event), but the river was able to maintain its channel visible in Figure 11e. As the river continued to flow, the deposited material partially blocking the Yarlung river gradually washed away, as seen in subsequent satellite images (Figures 11f–11h). Increased rainfall in the second half of August (Figure 11j) again seemed to trigger mass flow, leading to fan progradation (Figure 11f) and likely increased sediment yield from this area.

5. Discussion

5.1. Compositional Difference in PreF and PostF

The study period has two grain-size minima in PreF and PostF periods, which have similar grain-size distributions (Figure 2). The chemical composition in these two periods is similar with respect to higher Al and LOI contents, pointing to sheet silicates in general. However, a contrast in K, Mg, Fe, Ti and associated trace elements (Co, Sc, V, etc.; Figure 4b) is observed, which are enriched in PreF. This suggests enrichment of biotite, being supported by strong loadings for elements that are commonly hosted in biotite (Figure 5a) as well as bulk XRD analysis (Figure 6a).

The increase of Al and LOI in PostF does not correlate with other major elements (K, Mg, Fe). If the higher values of Al are to be explained by mineral enrichment only, kaolinite is a likely candidate, but the XRD data of the <2 μm grain-size fraction does not show any enrichment in specific clay minerals. In fact, the proportion of clay content in terms of grain size as well as clay minerals remain almost constant in PreF and PostF periods (Figure 6b). Thus, it can be inferred that the composition in these two periods is different mostly because of biotite enrichment in PreF (Figure 6a).

In addition to Al, a few elements such as Zn and Mn also show a higher concentration in PostF. These elements may be hosted in clay minerals and metal hydroxides/oxyhydroxides. A slight increase of chlorite in PostF (Figure 6a) may partially explain the Mn increase. Nevertheless, the increase in chlorite is not strong enough to

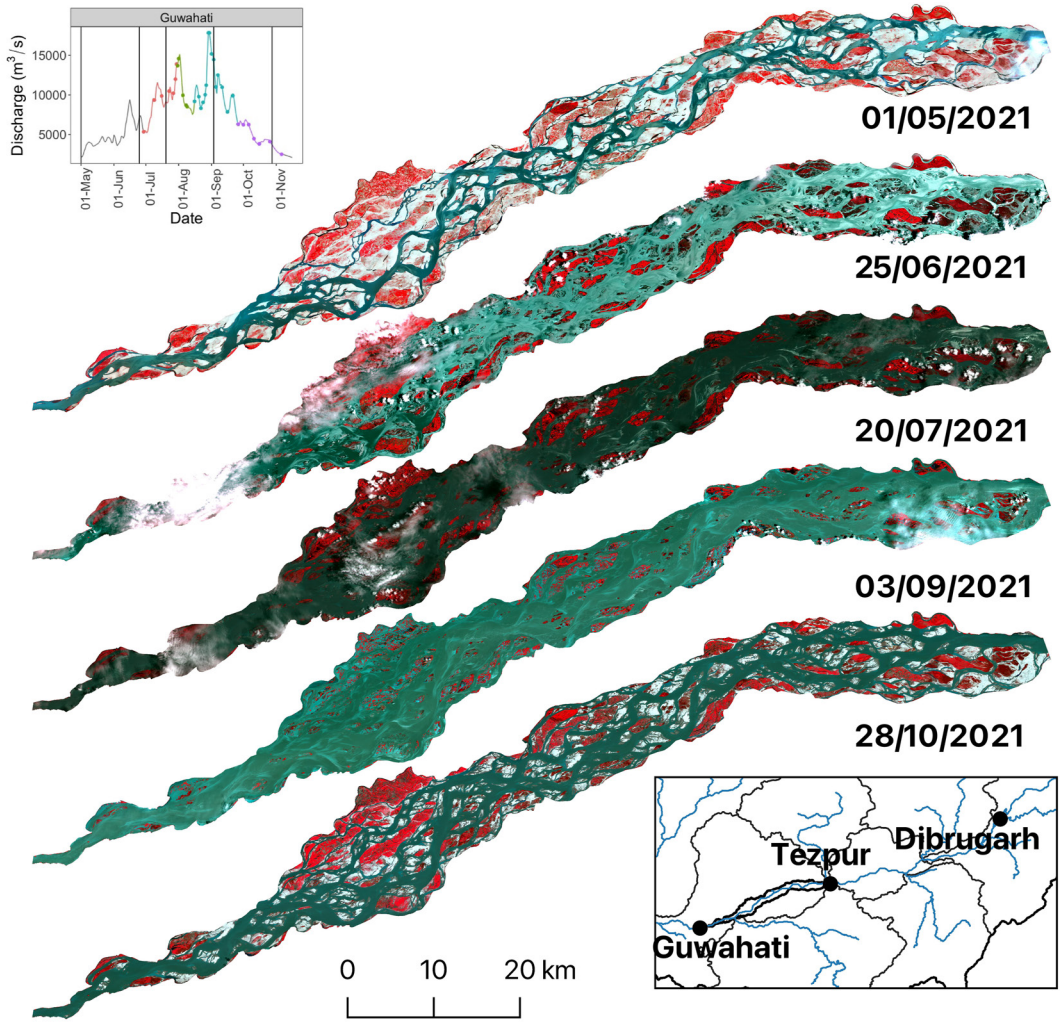

Figure 10. Optical satellite images of a section of braided Brahmaputra main trunk showing the submergence and reappearance of numerous sandbars during the flooding events. Satellite images are shown as false color composite. The red color represents the vegetation. Cyan color indicates unvegetated sandbars, and greenish blue indicates water. Vertical lines on the Guwahati discharge curve at the top left inset correspond to the dates of available cloud-free optical images. Bottom right inset shows the stretch of active channels between two morphological stable nodal points, that is, Guwahati and Tezpur (Nandi, Pradhan, Dutta, & Khatua, 2022).

significantly change other elements hosted in chlorite, such as Fe and Mg. Moreover, the Mn loading vectors are not associated with Al (Figure 5), indicating that clay minerals are not the only host of Mn; it might be available in the form of Mn hydroxides/oxyhydroxides, too (Garzanti et al., 2011). Overall, the PostF composition can be explained by the general grain-size effect on mineralogy and potential enrichment in metal oxyhydroxides, clay and other sheet silicates as a whole, but not any specific mineral enrichment like for biotite in the PreF period.

5.2. Provenance Shift in MonC Period

Certain ratios of heavy minerals have been used to constrain the lithological control regarding metamorphic sources based on the following reasoning:

1. Sillimanite (Sil), garnet (Grt) and clinopyroxene (Cpx) are stable over a broad temperature range, whereas epidote (Ep) is highly sensitive to temperature and disappears at 600°C at latest (e.g.,Bucher & Frey, 2002). Thus, considering Sil/Ep, Grt/Ep, and/or Cpx/Ep allow to put relative constrains on the contribution of high-temperature metamorphic rocks compared to those of lower-temperature.

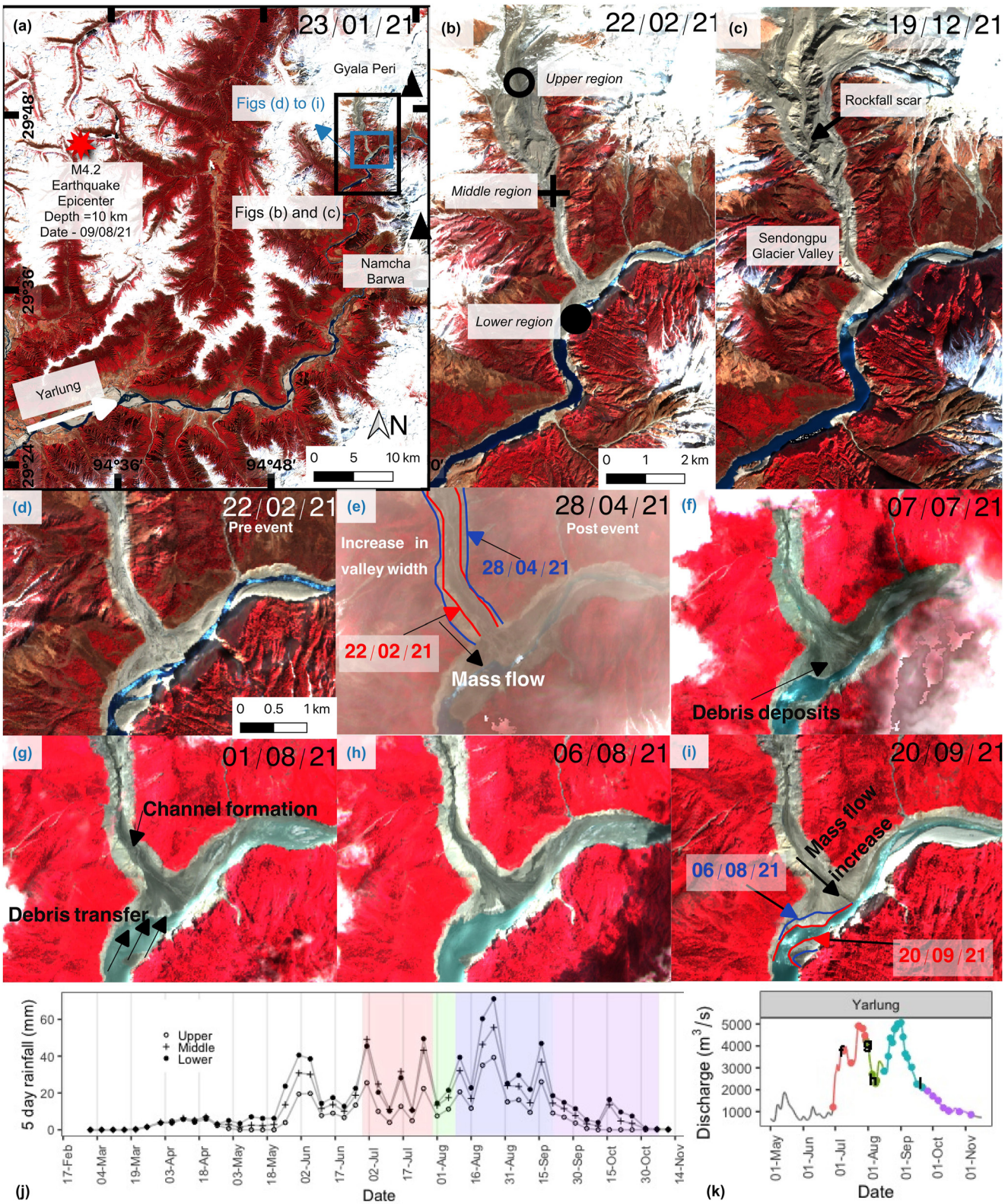
(a)
23/01/21
Gyala Peri
Figs (d) to (i)
Figs (b) and (c)
M4.2
Earthquake
Epicenter
Depth =10 km
Date - 09/08/21
Namcha
Barwa
Yarlung
29°48'
29°36'
29°24'
94°36'
94°48'
N
0 5 10 km
(b)
22/02/21
Upper region
Middle region
Lower region
0 1 2 km
(c)
19/12/21
Rockfall scar
Sendongpu
Glacier Valley
(d)
22/02/21
Pre event
0 0.5 1 km
(e)
28/04/21
Post event
Increase in
valley width
28/04/21
22/02/21
Mass flow
(f)
07/07/21
Debris deposits
(g)
01/08/21
Channel formation
Debris transfer
(h)
06/08/21
(i)
20/09/21
Mass flow
increase
06/08/21
20/09/21
5 day rainfall (mm)
Upper
Middle
Lower
17-Feb
04-Mar
19-Mar
03-Apr
18-Apr
03-May
18-May
02-Jun
17-Jun
02-Jul
17-Jul
01-Aug
16-Aug
31-Aug
15-Sep
30-Sep
15-Oct
30-Oct
14-Nov
Date
(j)
Yarlung
Discharge (m³/s)
01-May
01-Jun
01-Jul
01-Aug
01-Sep
01-Oct
01-Nov
Date
(k)

Figure 11.

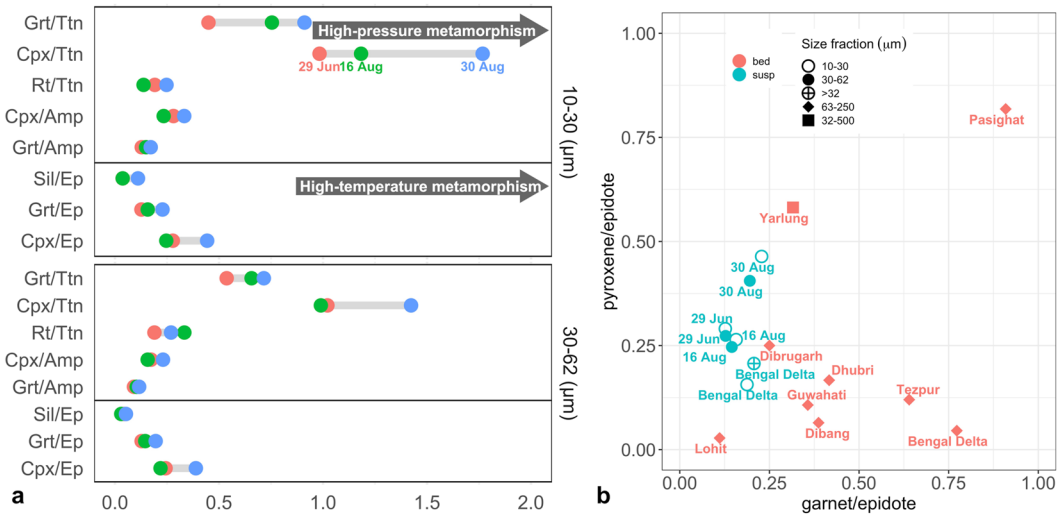

Figure 12. (a) Heavy mineral ratios for three samples of time series (color coded) and two grain-size fractions. Grt: garnet, Cpx: clinopyroxene, Rt: rutile, Ttn: titanite, Amp: amphibole, Ep: epidote-group minerals, Sil: sillimanite (b) Crossplot of the ratio of pyroxene to epidote versus the ratio of garnet to epidote. Data for different locations are taken from Garzanti et al. (2004), Garzanti et al. (2011), and Liang et al. (2022).

2. Amphibole (Amp) is stable in a broad pressure range from low pressures up to the amphibole-eclogite facies. In contrast, garnet is much more frequent in the high-pressure amphibolite and granulite facies, and clinopyroxene just appears by reaching the high-pressure amphibolite and granulite facies. Thus, an increase in their ratios (Cpx/Amp, Grt/Amp) will indicate a comparatively higher contribution from higher-pressure metamorphic rocks.
3. Likewise, titanite (Ttn) is mainly stable at lower pressures (typically <1 GPa) compared to rutile (Rt), garnet and clinopyroxene. Thus, their ratios (Grt/Ttn, Cpx/Ttn, Rt/Ttn) may also serve as an indicator for the relative contributions of higher-pressure metamorphic rocks compared to those of lower-pressure.

As shown in Figure 12a, above mentioned ratios are consistently highest in both grain-size fractions of the 30 August sample (blue color; except for Rt/Ttn in 30–62 μm). This indicates a higher contribution of high-pressure, high-temperature metamorphic sources compared to the other samples, which could be related to higher contributions from Subansiri and/or Siang. However, it is to be noted that even though clinopyroxene is a high-grade metamorphic mineral, it is also common in intermediate to mafic igneous lithology (Mange & Maurer, 1992). Since ratios including clinopyroxene consistently show a larger spread than those including garnet, this indicates an additionally increased contribution of intermediate-mafic igneous rocks. Both of these lithologies, that is, high-temperature/high-pressure metamorphic rocks and intermediate-mafic igneous rocks, exist in the Yarlung-Siang basin, where it drains the igneous THB and Gangdese belt and metamorphic rocks of Namcha Barwa—Gyala Peri massif (Figure 1). Higher values of pyroxene to epidote ratio (Px/Ep) and Grt/Ep at Yarlung and Pasighat, as reported for bed samples, support the occurrence of these lithologies in the upstream sub-basins particularly when compared to low Px/Ep ratios of Lohit and Dibang tributaries (Figure 12b). Overall, considering the fact that the Eastern Syntaxis provides a disproportionate amount of sediments (Table 2), peak monsoon sediments are characterized by an increased input from the Siang basin and igneous rocks of Yarlung. This is well in accordance with intense rainfall during the peak monsoon period over these sub-basins (Figure 8).

Figure 11. The evolution of the Sendongpu mass-wasting event that occurred on 22 March 2021, illustrated through a series of cloud-free satellite images. Panel (a) shows the location of the Sendongpu glacier valley on the western flank of Gyala Peri, as well as the epicenter of an earthquake that occurred on 9 August 2021, about 30 km away from the valley. Panels (b) and (c) reveal visible scars on the valley floor caused by mass-wasting event. The valley is divided into three regions, upper, middle and lower, corresponding to the three CHIRPS rainfall data grids, whose time series are shown in panel (j). Panels (d)–(i) capture the temporal changes in the valley following the mass-wasting event, including the partial blocking of the Yarlung river by the deposited debris (d and e), the flushing out of the debris (f–h), and the potential increase in debris flow (as indicated by fan progradation) due to heavy rainfall in the second half of August (i). Panel (j) shows the rainfall time series on the three CHIRPS grids covering the valley. Color in the background corresponds to the periods mentioned in the text, and panel (k) displays the discharge at Yarlung (Figure 9).

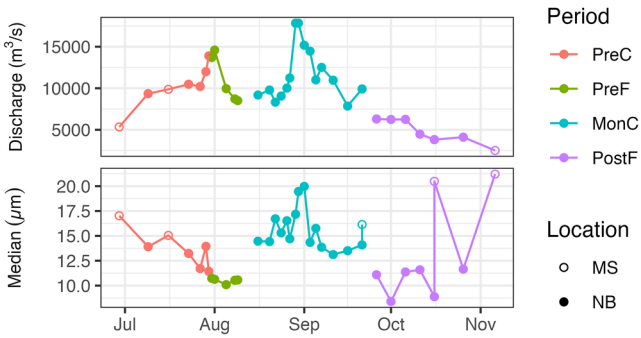

Figure 13. Daily discharge and grain size variability at Guwahati during study period.

5.3. Tracing Sediment Source in MonC: Insights From Sendongpu Mass-Wasting Processes

According to Kääb and Girod (2022), the 22 March 2021 Sendongpu mass-wasting event mobilized approximately 50×10^6 m^3 of material, and an additional 279×10^6 m^3 of material was eroded from the glacier bed between April and September 2021, with the majority occurring in June–August 2021. It is interesting to note that no significant re-deposition of this material was observed up to 6 km downstream. Our sampling period coincided with this timeframe, and it is noteworthy that the high rainfall event in the second half of August, visible in Figure 11i, coincided with the MonC period. This event triggered a significant amount of material mobilization, which may have contributed to the high-grade metamorphic inputs observed in our MonC sample, supported by the local geology of the region (Liu et al., 2019).

Furthermore, we observed that the discharges on 06/08/21 (2,492 m^3/s) and 20/09/21 (2,300 m^3/s) were comparable (Figure 11k), indicating that the deposit progression near the valley outlet visible on 20/09/21 was a fresh deposit and not due to the reappearance of an existing deposit. As the previous discharge and rainfall events did not coincide with the mass flow, it highlights the stochastic nature of such events.

Overall, while the exact source of the materials sampled during MonC cannot be constrained to a single source by our data, several factors lend support to the proposition and make it worthy of consideration. First, this area is known to be the primary source of sediments in the Brahmaputra. Second, the local geology of the region supports the presence of high-grade metamorphic inputs. Additionally, the temporal coincidence of the mass flow and our MonC sampling period is notable. Finally, estimates by Kääb and Girod (2022) indicate intense erosion in the Sendongpu valley with no nearby deposition, suggesting far-scale transport.

5.4. Implications for Sediment Transport Mechanism

The discharge and grain-size patterns in PreC and PreF periods differ from the MonC and PostF periods (Figures 9 and 13). The discharge from the end of June to the end of July (PreC) is increasing but the grain size for this period is overall decreasing. A coincidence of the falling limb of the discharge and the PreF period is notable. After the receding flood, discharge again increases from mid-August (MonC) along with the grain size; both are peaking at the end of August. Unlike PreC and PreF, the grain size and discharge trends are similar in MonC and PostF periods (except for the midstream samples in the PostF).

The reverse trend of grain size and discharge in the PreC and PreF periods raises the possibility of sediment supply control. It is stressed that the sediment concentration is higher in PreF than in PostF (Figure 3). Thus, the supply control was not in terms of the quantity of sediments transported; rather, supply was limited to specific grain size and related mineralogy and chemistry. Figure 10 shows that the exposed unvegetated sandbars were already mostly submerged even before PreC period. PreC and previous flooding events might have re-suspended the bed sediments from numerous sandbars, as illustrated in Figure 14. The sandbar sediments are hydrodynamically sorted, sand-sized deposits (Dixit et al., 2021) which are enriched in quartz, feldspar and mica, with biotite prevailing over muscovite (Garzanti et al., 2004, 2010). Micas are enriched toward the finer tails of overbank deposits through winnowing during floods (Gemignani et al., 2018). These materials might be mobilized from the sandbars during the first few flooding spells in higher rainfall and flow conditions. Once mobilized, they are progressively hydrodynamically sorted in the water column as the discharge and channel depth increase by the end of July. After the peak discharge at the end of July, the flood receded in the PreF period while the river stayed morphologically stable. This allows settling down coarser material and enriching sheet silicates, especially biotite, in the suspended sediments. The grain size does not decrease further, and samples become better sorted with a lower standard deviation of the grain-size distribution (Figure 2b).

In MonC period, sediments were most likely to be transported from the primary sources in the eastern part of the basin, including Yarlung—Siang and potentially the Sendongpu glacier valley, which received concentrated rainfall in this period (Figures 8 and 11j). While there may have been some contribution from these primary sources in the PreF and PreC periods, the floodplains were the dominant source of sediment during these times. Once the

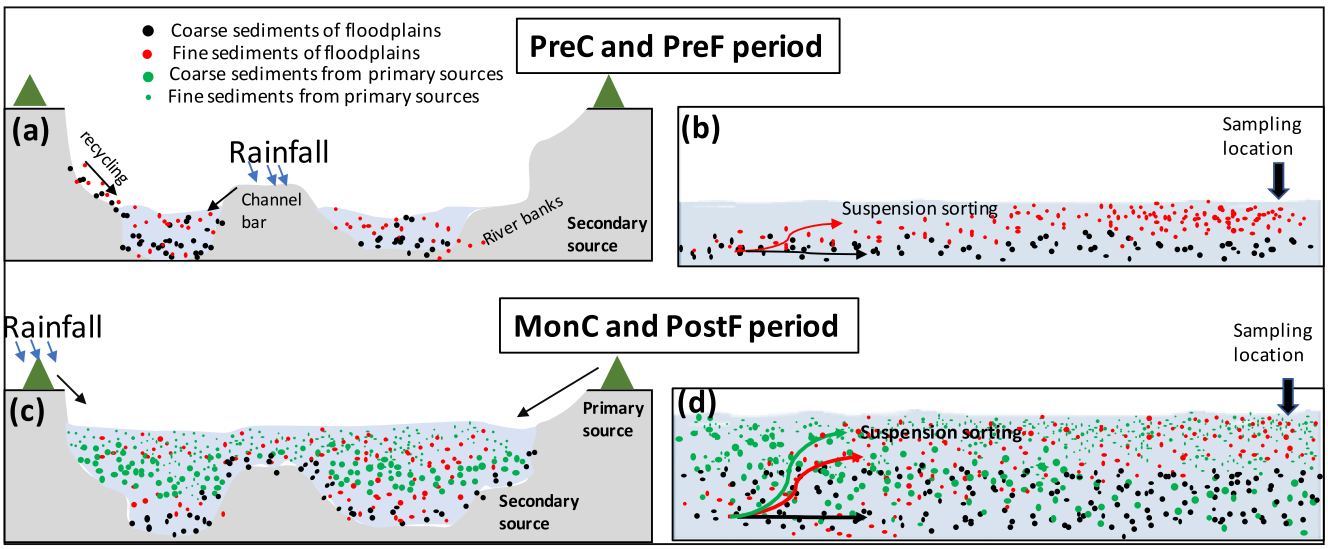

Figure 14. Sediment transport mechanism in two flooding periods. (a) and (c) represent cross-section of the channel in PreC-PreF and MonC-PostF periods, respectively. (b) and (d) illustrate the longitudinal sediment transport mechanism in respective periods. Black dots represent coarse-grained quartz and feldspar of channel bar and river bank as a secondary source of suspended sediments. Red dots are fine-grained sheet silicates of bank and bar deposits. Green dots are fresh sediments from primary sources.

river attained a morphological stable channel with fewer inputs from the floodplain in MonC (see 03/09/21 in Figure 10), signatures of the primary sources become evident. Notably, we sampled top water surface suspended sediments that can be characterized as wash load, which by definition can remain suspended and travel long distances. Thus, the finest material generated from upstream primary sources may reach far downstream. Once the sediments are mobilized from these primary sources, they are progressively sorted in the water column with increasing transport distance (Figure 14). The PostF period then acted as a post-monsoon relaxation period in terms of grain size and discharge (Figure 13), vastly keeping the compositional signature of low biotite to quartz ratio along with low Fe, Mg, Ti, and K contents compared to PreF.

5.5. Suggestions on Sediment Sampling Strategies for Provenance Studies

Previous sediment provenance models have been based on individual samples collected primarily during the monsoon periods. Our study highlights the clear compositional variations even within a single monsoon period due to factors such as floodplain morphology, rainfall distribution, and large-scale mass-wasting events. It is therefore important to consider these factors during sampling to avoid biases in calculations and interpretations. If the objective of the sampling is to determine and quantify the sources from different geological units, it is of first-order importance to solely compare samples that have been taken in a short period of time to minimize bias related to intra-seasonal variability of sediment composition. In addition, sampling during the initial flood periods should be avoided. Instead, sampling during subsequent flooding events should be interpreted in relation to the rainfall distribution over different parts of the basin.

Collecting a representative sample can be challenging in large, braided rivers with multiple channels. Midstream samples are considered to be the most representative, but due to the complexity of the river, its often not feasible to collect them. However, strategic locations can be selected where the river is geographically forced into narrower channels. The Brahmaputra river has three such nodes, namely Tezpur, Guwahati (Figure 10), and Goalpara (not shown in figures, approximately 100 km upstream of Dhubri). At these locations, the river almost perennially flows in a single-channel system, and during high discharge periods, near-bank samples can also carry representative compositions due to strong mixing with the midstream section.

6. Conclusion

We observed changes in sediment composition mainly related to two flooding events during the sampling period from 29 June 2021 to 07 November 2021. Our chemical, mineralogical and hydrological data suggest that the first flooding event brought the sediments from the exposed sandbars and/or banks in floodplains. The sandbar sediments are hydraulically sorted deposits, depleted in the finer grain-size fractions, mostly enriched in quartz, feldspar and mica. They are easily mobilized from the exposed bed, and once entrained, they are further sorted in the water column, enriching micas at the top water surface. Even though rainfall and discharge of major tributaries and subsequent sediment generation might be considerable, entrainment and sediment transport from exposed sandbars dominate other sources. After the first flooding event, the submergence of floodplain sandbars causes the river to shift to a largely stable single-channel system. This change leads to an increase in sediment input from primary sources, such as the Yarlung-Siang, and potentially the Sendongpu glacier valley, a location prone to frequent mass-wasting events. Thus, in the second flooding event, the river carried relatively higher proportion of sediments derived from primary non-hydraulic sorted sources compared to the first flooding event. To conclude, multiple flooding events can comprise different proportions of sediment sources and transport processes. This temporal variability applies not only to the inter-seasonal variation as previously observed (Golombek et al., 2021; Jian et al., 2020) but also to the variations within a single season. The temporal variation observed in this case study poses constraints on the interpretation of compositional differences in terms of sediment provenance, and should be considered in studies of modern drainage basins as well as ancient sediment routing systems.

Data Availability Statement

The grain-size distributions, chemical and mineralogical data used in this work are made available on Zenodo, https://doi.org/10.5281/zenodo.7588054 (Dixit et al., 2023). Discharge data from Global Flood Monitoring System can be accessed from http://flood.umd.edu/.

Acknowledgments
This research was supported by the NAMASTE + exchange program to A.D. funded by the DAAD and the German Ministry of Education and Research. Analytical lab work has been performed at the Geoscience Center Göttingen, Dept. of Sedimentology and Environmental Geology. A.D. would like to express gratitude to Dr. Bernhard Peucker-Ehrenbrink for the earliest discussions of the research idea. We would like to thank Dr. Huan Wu and Dr. Naijun Zhaou for providing the Global Flood Monitoring System (GFMS) discharge data. We are also grateful to Dr. Keno Lünsdorf and Lena Weimann (Göttingen) for their help with heavy-mineral analysis. Sourav and Shreya (Guwahati) are thanked for their help in sample collection. Open Access funding enabled and organized by Projekt DEAL.

References

Acharyya, S. (2007). Evolution of the Himalayan Paleogene foreland basin, influence of its litho-packet on the formation of thrust-related domes and windows in the eastern Himalayas–a review. *Journal of Asian Earth Sciences*, *31*(1), 1–17. https://doi.org/10.1016/j.jseaes.2007.03.007

Andò, S. (2020). Gravimetric separation of heavy minerals in sediments and rocks. *Minerals*, *10*(3), 273. https://doi.org/10.3390/min10030273

Biscay, P. E. (1965). Mineralogy and sedimentation of recent deep-sea clay in the Atlantic Ocean and adjacent seas and oceans. *Geological Society of America Bulletin*, *76*(7), 803–832. https://doi.org/10.1130/0016-7606(1965)76[803:masord]2.0.co;2

Brunnschweiler, R. O. (1966). On the geology of the Indoburman ranges: (Arakan Coast and Yoma, Chin Hills, Naga Hills). *Journal of the Geological Society of Australia*, *13*(1), 137–194. https://doi.org/10.1080/00167616608728608

Bucher, K., & Frey, M. (2002). *Petrogenesis of metamorphic rocks*. Springer Science & Business Media.

Burg, J.-P., Nievergelt, P., Oberli, F., Seward, D., Davy, P., Maurin, J.-C., et al. (1998). The Namche Barwa syntaxis: Evidence for exhumation related to compressional crustal folding. *Journal of Asian Earth Sciences*, *16*(2–3), 239–252. https://doi.org/10.1016/s0743-9547(98)00002-6

Dickinson, W. R. (1985). Interpreting provenance relations from detrital modes of sandstones. In G. Zuffa (Ed.), *Provenance of arenites* (pp. 333–361). Springer. https://doi.org/10.1007/978-94-017-2809-6_15

Dixit, A., Kumar, S., Mahanta, C., Chaudhari, S., & Rana, M. (2021). Application of grain-size end-member modelling in bed sediments of the Brahmaputra River. In *AGU fall meeting abstracts* (Vol. 2021, pp. EP34D–03).

Dixit, A., von Eynatten, H., Schönig, J., Karius, V., Mahanta, C., & Dutta, S. (2023). Data for Intra-seasonal variability of sediment provenance in the Brahmaputra basin. *Zenodo*. https://doi.org/10.5281/zenodo.7588054

Doebelin, N., & Kleeberg, R. (2015). Profex: A graphical user interface for the Rietveld refinement program BGMN. *Journal of Applied Crystallography*, *48*(5), 1573–1580. https://doi.org/10.1107/s1600576715014685

Enkelmann, E., Ehlers, T., Zeitler, P., & Hallet, B. (2011). Denudation of the Namche Barwa antiform, eastern Himalaya. *Earth and Planetary Science Letters*, *307*(3–4), 323–333. https://doi.org/10.1016/j.epsl.2011.05.004

Finnegan, N. J., Hallet, B., Montgomery, D. R., Zeitler, P. K., Stone, J. O., Anders, A. M., & Yuping, L. (2008). Coupling of rock uplift and river incision in the Namche Barwa-Gyala Peri massif, Tibet. *Bulletin of the Geological Society of America*, *120*(1–2), 142–155. https://doi.org/10.1130/B26224.1

Funk, C., Peterson, P., Landsfeld, M., Pedreros, D., Verdin, J., Shukla, S., et al. (2015). The climate hazards infrared precipitation with stations—A new environmental record for monitoring extremes. *Scientific Data*, *2*(1), 1–21. https://doi.org/10.1038/sdata.2015.66

Galy, A., & France-Lanord, C. (2001). Higher erosion rates in the Himalaya: Geochemical constraints on riverine fluxes. *Geology*, *29*(1), 23–26. https://doi.org/10.1130/0091-7613(2001)029⟨0023:HERITH⟩2.0.CO;2

Garzanti, E. (2019). The Himalayan foreland basin from collision onset to the present: A sedimentary–petrology perspective. *Geological Society, London, Special Publications*, *483*(1), 65–122. https://doi.org/10.1144/sp483.17

Garzanti, E., & Andò, S. (2007). Plate tectonics and heavy mineral suites of modern sands. *Developments in Sedimentology*, *58*, 741–763.

Garzanti, E., Andó, S., France-Lanord, C., Censi, P., Vignola, P., Galy, V., & Lupker, M. (2011). Mineralogical and chemical variability of fluvial sediments 2. Suspended-load silt (Ganga–Brahmaputra, Bangladesh). *Earth and Planetary Science Letters*, *302*(1–2), 107–120. https://doi.org/10.1016/j.epsl.2010.11.043

Garzanti, E., Andò, S., France-Lanord, C., Vezzoli, G., Censi, P., Galy, V., & Najman, Y. (2010). Mineralogical and chemical variability of fluvial sediments. 1. Bedload sand (Ganga-Brahmaputra, Bangladesh). *Earth and Planetary Science Letters*, *299*(3–4), 368–381. https://doi.org/10.1016/j.epsl.2010.09.017

Garzanti, E., Vezzoli, G., Andò, S., France-Lanord, C., Singh, S. K., & Foster, G. (2004). Sand petrology and focused erosion in collision orogens: The Brahmaputra case. *Earth and Planetary Science Letters*, *220*(1–2), 157–174. https://doi.org/10.1016/S0012-821X(04)00035-4

Gemignani, L., van der Beek, P., Braun, J., Najman, Y., Bernet, M., Garzanti, E., & Wijbrans, J. (2018). Downstream evolution of the thermochronologic age signal in the Brahmaputra catchment (eastern Himalaya): Implications for the detrital record of erosion. *Earth and Planetary Science Letters*, *499*, 48–61. https://doi.org/10.1016/j.epsl.2018.07.019

Golombek, N. Y., Scheingross, J. S., Repasch, M. N., Hovius, N., Menges, J., Sachse, D., et al. (2021). Fluvial organic carbon composition regulated by seasonal variability in lowland river migration and water discharge. *Geophysical Research Letters*, *48*(24), e2021GL093416. https://doi.org/10.1029/2021gl093416

Goswami, D. C. (1985). Brahmaputra River, Assam, India: Physiography, basin denudation, and channel aggradation. *Water Resources Research*, *21*(7), 959–978. https://doi.org/10.1029/wr021i007p00959

Gururajan, N., & Choudhuri, B. (2003). Geology and tectonic history of the lohit valley, eastern Arunachal Pradesh, India. *Journal of Asian Earth Sciences*, *21*(7), 731–741. https://doi.org/10.1016/s1367-9120(02)00040-8

Imai, N., Terashima, S., Itoh, S., & Ando, A. (1995). 1994 compilation of analytical data for minor and trace elements in seventeen GSJ geochemical reference samples,"igneous rock series". *Geostandards Newsletter*, *19*(2), 135–213. https://doi.org/10.1111/j.1751-908x.1995.tb00158.x

Immerzeel, W. W., van Beek, L. P. H., & Bierkens, M. F. P. (2010). Climate change will affect the Asian water towers. *Science*, *328*(5984), 1382–1385. https://doi.org/10.1126/science.1183188

Islam, M. R., Begum, S. F., Yamaguchi, Y., & Ogawa, K. (1999). The Ganges and Brahmaputra rivers in Bangladesh: Basin denudation and sedimentation. *Hydrological Processes*, *13*(17), 2907–2923. https://doi.org/10.1002/(SICI)1099-1085(19991215)13:17⟨2907::AID-HYP906⟩3.0.CO;2-E

Jian, X., Yang, S., Hong, D., Liang, H., Zhang, S., Fu, H., & Zhang, W. (2020). Seasonal geochemical heterogeneity of sediments from a subtropical mountainous river in se China. *Marine Geology*, *422*, 106120. https://doi.org/10.1016/j.margeo.2020.106120

Johnsson, M. J. (1993). The system controlling the composition of clastic sediments. In *Processes controlling the composition of clastic sediments* (pp. 1–20). Geological Society of America Special Paper. https://doi.org/10.1130/spe284-p1

Kääb, A., & Girod, L. (2022). Brief communication: Rapid˜ 335 10 6 m 3 bed erosion after detachment of the Sedongpu Glacier (Tibet). *The Cryosphere Discussions*, *1–9*.

Kääb, A., Jacquemart, M., Gilbert, A., Leinss, S., Girod, L., Huggel, C., et al. (2021). Sudden large-volume detachments of low-angle mountain glaciers–more frequent than thought? *The Cryosphere*, *15*(4), 1751–1785. https://doi.org/10.5194/tc-15-1751-2021

Karmaker, T., & Dutta, S. (2010). Generation of synthetic seasonal hydrographs for a large river basin. *Journal of Hydrology*, *381*(3–4), 287–296. https://doi.org/10.1016/j.jhydrol.2009.12.001

Karmaker, T., Ramprasad, Y., & Dutta, S. (2010). Sediment transport in an active erodible channel bend of Brahmaputra River. *Sadhana*, *35*(6), 693–706. https://doi.org/10.1007/s12046-010-0052-7

Kaser, G., Großhauser, M., & Marzeion, B. (2010). Contribution potential of glaciers to water availability in different climate regimes. *Proceedings of the National Academy of Sciences of the United States of America*, *107*(47), 20223–20227. https://doi.org/10.1073/pnas.1008162107

Khan, M. H. R., Liu, J., Liu, S., Seddique, A. A., Cao, L., & Rahman, A. (2019). Clay mineral compositions in surface sediments of the Ganges-Brahmaputra-Meghna river system of Bengal Basin, Bangladesh. *Marine Geology*, *412*, 27–36. https://doi.org/10.1016/j.margeo.2019.03.007

Lafuente, B., Downs, R. T., Yang, H., & Stone, N. (2015). The power of databases: The RRUFF project. In *Highlights in mineralogical crystallography* (pp. 1–30). DE GRUYTER. https://doi.org/10.1515/9783110417104-003

Lang, K. A., Huntington, K. W., & Montgomery, D. R. (2013). Erosion of the Tsangpo Gorge by megafloods, eastern Himalaya. *Geology*, *41*(9), 1003–1006. https://doi.org/10.1130/G34693.1

Larsen, I. J., & Montgomery, D. R. (2012). Landslide erosion coupled to tectonics and river incision. *Nature Geoscience*, *5*(7), 468–473. https://doi.org/10.1038/ngeo1479

Liang, W., Garzanti, E., Hu, X., Resentini, A., Vezzoli, G., & Yao, W. (2022). Tracing erosion patterns in South Tibet: Balancing sediment supply to the Yarlung Tsangpo from the Himalaya versus Lhasa block. *Basin Research*, *34*(1), 411–439. https://doi.org/10.1111/bre.12625

Liu, C., Lü, J., Tong, L., Chen, H., Liu, Q., Xiao, R., & Tu, J. (2019). Research on glacial/rock fall-landslide-debris flows in Sedongpu basin along Yarlung Zangbo River in Tibet. *Geology in China*, *46*(2), 219–234.

Lünsdorf, N. K., Kalies, J., Ahlers, P., Dunkl, I., & von Eynatten, H. (2019). Semi-automated heavy-mineral analysis by Raman spectroscopy. *Minerals*, *9*(7), 385. https://doi.org/10.3390/min9070385

Lupker, M., France-Lanord, C., Galy, V., Lavé, J., Gaillardet, J., Gajurel, A. P., et al. (2012). Predominant floodplain over mountain weathering of Himalayan sediments (Ganga basin). *Geochimica et Cosmochimica Acta*, *84*, 410–432. https://doi.org/10.1016/j.gca.2012.02.001

Lupker, M., France-Lanord, C., Lavé, J., Bouchez, J., Galy, V., Métivier, F., et al. (2011). A rouse-based method to integrate the chemical composition of river sediments: Application to the ganga basin. *Journal of Geophysical Research*, *116*(F4), F04012. https://doi.org/10.1029/2010jf001947

Lupker, M., Lavé, J., France-Lanord, C., Christl, M., Bourlès, D., Carcaillet, J., et al. (2017). 10 be systematics in the Tsangpo-Brahmaputra catchment: The cosmogenic nuclide legacy of the eastern Himalayan Syntaxis. *Earth Surface Dynamics*, *5*(3), 429–449. https://doi.org/10.5194/esurf-5-429-2017

Mange, M. A., & Maurer, H. F. W. (1992). *Heavy minerals in color*. Springer Netherlands. https://doi.org/10.1007/978-94-011-2308-2

Milliman, J. D., & Farnsworth, K. L. (2011). *River discharge to the coastal ocean*. Cambridge University Press. https://doi.org/10.1017/CBO9780511781247

Misra, D. (2009). Litho-tectonic sequence and their regional correlation along the lohit and Dibang valleys, eastern Arunachal Pradesh. *Journal of the Geological Society of India*, *73*(2), 213–219. https://doi.org/10.1007/s12594-009-0077-x

Mitra, S., & Mitra, S. (2001). Tectonic setting of the Precambrian of the north-eastern India (Meghalaya Plateau) and age of the Shillong group of rocks. *Geological Survey of India Special Publication*, *64*, 653–658.

Nandi, K. K., Pradhan, C., Dutta, S., & Khatua, K. K. (2022). How dynamic is the Brahmaputra? Understanding the process–form–vegetation interactions for hierarchies of energy dissipation. *Ecohydrology*, *15*(3), e2416. https://doi.org/10.1002/eco.2416

Nandi, K. K., Pradhan, C., Padhee, S., Dutta, S., & Khatua, K. K. (2022). Understanding the entropy-based morphological variability and energy expenditure mechanism of a large braided river system. *Journal of Hydrology*, *615*, 128662. https://doi.org/10.1016/j.jhydrol.2022.128662

Nesbitt, H. W., Fedo, C. M., & Young, G. M. (1997). Quartz and feldspar stability, steady and non-steady-state weathering, and petrogenesis of siliciclastic sands and muds. *The Journal of Geology*, *105*(2), 173–192. https://doi.org/10.1086/515908

Panda, S., Kumar, A., Das, S., Devrani, R., Rai, S., Prakash, K., & Srivastava, P. (2020). Chronology and sediment provenance of extreme floods of Siang River (Tsangpo-Brahmaputra River valley), northeast Himalaya. *Earth Surface Processes and Landforms*, *45*(11), 2495–2511. https://doi.org/10.1002/esp.4893

Rai, S. K., & Singh, S. K. (2007). Temporal variation in Sr and $^{87}Sr/^{86}Sr$ of the Brahmaputra: Implications for annual fluxes and tracking flash floods through chemical and isotope composition. *Geochemistry, Geophysics, Geosystems*, *8*, Q08008. https://doi.org/10.1029/2007GC001610

Rodriguez, J. D., Westenberger, B. J., Buhse, L. F., & Kauffman, J. F. (2011). Quantitative evaluation of the sensitivity of library-based Raman spectral correlation methods. *Analytical Chemistry*, *83*(11), 4061–4067. https://doi.org/10.1021/ac200040b

Salvi, D., Mathew, G., & Kohn, B. (2017). Rapid exhumation of the upper Siang Valley, Arunachal Himalaya since the Pliocene. *Geomorphology*, *284*, 238–249. https://doi.org/10.1016/j.geomorph.2016.09.032

Salvi, D., Mathew, G., Kohn, B., Pande, K., & Borgohain, B. (2020). Thermochronological insights into the thermotectonic evolution of Mishmi hills across the Dibang Valley, ne Himalayan Syntaxis. *Journal of Asian Earth Sciences*, *190*, 104158. https://doi.org/10.1016/j.jseaes.2019.104158

Samanta, A., Tripathy, G. R., & Das, R. (2019). Temporal variations in water chemistry of the (Lower) Brahmaputra River: Implications to seasonality in mineral weathering temporal variations in water chemistry of the (Lower) Brahmaputra River: Implications to seasonality in mineral weathering. *Geochemistry, Geophysics, Geosystems*, *20*(6), 2769–2785. https://doi.org/10.1029/2018GC008047

Sarma, J. (2004). An overview of the Brahmaputra river system. In *The Brahmaputra basin water resources* (pp. 72–87). Springer Netherlands. https://doi.org/10.1007/978-94-017-0540-0

Sarma, J. (2005). Fluvial process and morphology of the Brahmaputra River in Assam, India. *Geomorphology*, *70*(3–4), 226–256. https://doi.org/10.1016/j.geomorph.2005.02.007

Shi, X., Zhang, F., Lu, X., Wang, Z., Gong, T., Wang, G., & Zhang, H. (2018). Spatiotemporal variations of suspended sediment transport in the upstream and midstream of the Yarlung Tsangpo river (the upper Brahmaputra), China. *Earth Surface Processes and Landforms*, *43*(2), 432–443. https://doi.org/10.1002/esp.4258

Singh, S. K. (2006). Spatial variability in erosion in the Brahmaputra basin: Causes and impacts. *Current Science*, *90*(10), 1272–1275.

Singh, S. K. (2007). Erosion and weathering in the Brahmaputra River system. In A. Gupta (Ed.), *Large rivers: Geomorphology and management* (pp. 373–393). Wiley Blackwell. https://doi.org/10.1002/9780470723722.ch18

Singh, S. K., & France-Lanord, C. (2002). Tracing the distribution of erosion in the Brahmaputra watershed from isotopic compositions of stream sediments. *Earth and Planetary Science Letters*, *202*(3–4), 645–662. https://doi.org/10.1016/S0012-821X(02)00822-1

Singh, V., Sharma, N., & Ojha, C. S. P. (2004). *The Brahmaputra basin water resources* (Vol. 47). Springer Science & Business Media.

Turzewski, M. D., Huntington, K. W., Licht, A., & Lang, K. A. (2020). Provenance and erosional impact of quaternary megafloods through the Yarlung-Tsangpo gorge from zircon U-Pb geochronology of flood deposits, eastern Himalaya. *Earth and Planetary Science Letters*, *535*, 116113. https://doi.org/10.1016/j.epsl.2020.116113

Uddin, A., Kumar, P., Sarma, J. N., & Akhter, S. H. (2007). Heavy mineral constraints on the provenance of Cenozoic sediments from the foreland basins of Assam and Bangladesh: Erosional history of the eastern Himalayas and the indo-Burman ranges. *Developments in Sedimentology*, *58*, 823–847.

von Eynatten, H., Tolosana-Delgado, R., Karius, V., Bachmann, K., & Caracciolo, L. (2016). Sediment generation in humid Mediterranean setting: Grain-size and source-rock control on sediment geochemistry and mineralogy (Sila massif, Calabria). *Sedimentary Geology*, *336*, 68–80. https://doi.org/10.1016/j.sedgeo.2015.10.008

Wasson, R., Acharjee, S., & Rakshit, R. (2022). Towards identification of sediment sources, and processes of sediment production, in the Yarlung-Tsangpo-Brahmaputra river catchment for reduction of fluvial sediment loads. *Earth-Science Reviews*, *226*, 103932. https://doi.org/10.1016/j.earscirev.2022.103932

Weltje, G. J., & von Eynatten, H. (2004). Quantitative provenance analysis of sediments: Review and outlook. *Sedimentary Geology*, *171*(1–4), 1–11. https://doi.org/10.1016/j.sedgeo.2004.05.007

Wen, D., Liu, D., Chung, S., Chu, M., Ji, J., Zhang, Q., et al. (2008). Zircon SHRIMP U–Pb ages of the Gangdese batholith and implications for Neotethyan subduction in southern Tibet. *Chemical Geology*, *252*(3–4), 191–201. https://doi.org/10.1016/j.chemgeo.2008.03.003

Wu, H., Adler, R. F., Tian, Y., Huffman, G. J., Li, H., & Wang, J. (2014). Real-time global flood estimation using satellite-based precipitation and a coupled land surface and routing model. *Water Resources Research*, *50*(3), 2693–2717. https://doi.org/10.1002/2013wr014710

Yin, A., & Harrison, T. M. (2000). Geologic evolution of the Himalayan-Tibetan orogen. *Annual Review of Earth and Planetary Sciences*, *28*(1), 211–280. https://doi.org/10.1146/annurev.earth.28.1.211

Zhao, C., Yang, W., Westoby, M., An, B., Wu, G., Wang, W., et al. (2022). Brief communication: An approximately 50 mm^3 ice-rock avalanche on 22 march 2021 in the Sedongpu valley, southeastern Tibetan Plateau. *The Cryosphere*, *16*(4), 1333–1340. https://doi.org/10.5194/tc-16-1333-2022

Zhu, D.-C., Zhao, Z.-D., Niu, Y., Dilek, Y., Hou, Z.-Q., & Mo, X.-X. (2013). The origin and pre-Cenozoic evolution of the Tibetan Plateau. *Gondwana Research*, *23*(4), 1429–1454. https://doi.org/10.1016/j.gr.2012.02.002